Chapter 2
Velocity-Based Formulations for Compressible Materials

In this chapter two velocity-based finite element formulations for compressible materials are presented, namely the Velocity (V) and the mixed Velocity–Pressure (VP) formulations. For both schemes the linear momentum equations are solved iteratively for the velocity increments. The linearization of the governing equations is performed without specifying any constitutive law. The aim of this chapter is to maintain as much as possible the generality of the algorithms, leaving the formulations open to different material models. It will be shown that the only requirement demanded to the constitutive laws is that the rate of stress must be linearly related with the rate of deformation.

There are several reasons that justify the presentation of the Velocity formulation. First of all, the tangent matrix of the linear momentum equations for the Velocity formulation holds also for the here proposed mixed Velocity–Pressure formulation. Furthermore, the Velocity formulation is useful for making some interesting and didactic comparisons with the mixed formulations.

After deriving the solution scheme for the Velocity formulation, the mixed Velocity–Pressure method is presented. The governing equations are the linear momentum and the linear pressure-deformation rate equations. The latter is called continuity, or mass balance, equation for its similarity with the incompressibility constraint of the Navier–Stokes problem. As for the velocity scheme, in the mixed formulation the constitutive law is not specified. In Sect. 2.3 the hypoelastic–plastic model is presented and this constitutive law is inserted in both the Velocity and the mixed Velocity–Pressure schemes. The incremental solution scheme is explained in detail for both formulations. At the end of the chapter some validation examples for hypoelastic–plastic solids in statics as in dynamics are given.

A. Franci, *Unified Lagrangian Formulation for Fluid and Solid Mechanics, Fluid-Structure Interaction and Coupled Thermal Problems Using the PFEM*, Springer Theses, DOI 10.1007/978-3-319-45662-1_2

2.1 Velocity Formulation

In this section, the Velocity formulation for solving transient problems for a general continuum is derived. The governing equations are the linear momentum equations and they are derived in the updated Lagrangian (UL) framework. This means that the governing equations are integrated over the unknown configuration Ω (the so-called updated configuration). As a consequence, the space derivatives for the UL description are computed with respect to the spatial coordinates.

2.1.1 From the Local Form to the Spatial Semi-discretization

In this section the spatial semi-discretization of the linear momentum equations is derived.

For a general continuum, the local form of the linear momentum equations using the UL description reads

$$\rho(\mathbf{X},t)\frac{\partial \boldsymbol{v}(\mathbf{X},t)}{\partial t} - \frac{\partial \boldsymbol{\sigma}(\mathbf{X},t)}{\partial \mathbf{x}} - \boldsymbol{b}(\mathbf{X},t) = 0 \qquad in\ \Omega \times (0,T) \tag{2.1}$$

where ρ is the density of the material, $\boldsymbol{v}$ are the velocity vector, $\boldsymbol{\sigma}$ is the Cauchy stress tensor and $\boldsymbol{b}$ is the body force vector. The variables within the brackets are the independent variables: $\mathbf{X}$ are the Lagrangian or material coordinates vector, $\mathbf{x}$ the Eulerian or spatial coordinates vector and t is the time. For simplicity, in what follows the independent variables are not specified. The spatial and material coordinates are related through the motion tensor $\boldsymbol{\Phi}$ as

$$\mathbf{x} = \boldsymbol{\Phi}(\mathbf{X},t), \qquad \mathbf{X} = \boldsymbol{\Phi}^{-1}(\mathbf{x},t) \tag{2.2}$$

The set of governing equations is completed by the following conditions at the Dirichlet (Γ_v) and Neumann (Γ_t) boundaries

$$v_i - v_i^p = 0 \qquad \text{on } \Gamma_v \tag{2.3}$$

$$\sigma_{ij} n_j - t_i^p = 0 \qquad \text{on } \Gamma_t \tag{2.4}$$

where v_i^p and t_i^p are the prescribed velocities and the prescribed tractions, respectively, and $\boldsymbol{n}$ is the unit normal vector.

In the following summation of terms for repeated indices is assumed, unless otherwise specified.

The spaces for the trial and test functions are defined, respectively, as

$$v_i \in U, \qquad U = \{v_i | v_i \in \boldsymbol{C}^0,\ v_i = v_i^p\ on\ \Gamma_v\} \tag{2.5}$$

$$w_i \in U_0, \qquad U_0 = \{w_i | w_i \in \boldsymbol{C}^0,\ w_i = 0\ on\ \Gamma_v\} \tag{2.6}$$

Multiplying Eqs. (2.1) by the test functions and integrating over the updated configuration domain, the following global integral form is obtained

$$\int_\Omega w_i \left(\rho \dot{v}_i - \frac{\partial \sigma_{ij}}{\partial x_j} - b_i\right) d\Omega = 0 \tag{2.7}$$

where the symbol $\dot{(\cdot)}$ represents the material time derivative.

Integrating by parts the term involving σ_{ij} in Eq. (2.7) and using the Neumann boundary conditions (2.4) yields the weak variational form of the momentum equations as

$$\int_\Omega w_i \rho \dot{v}_i d\Omega + \int_\Omega \frac{\partial w_i}{\partial x_j} \sigma_{ij} d\Omega - \int_\Omega w_i b_i d\Omega - \int_{\Gamma_t} w_i t_i^p d\Gamma = 0 \tag{2.8}$$

Equation (2.8) is the standard form of the Principle of Virtual Power [1].

The spatial discretization is introduced using the classical FEM-Galerkin procedure [2]. Hence both the trial and the test functions are interpolated in space in terms of their nodal values by means of the same shape functions $\boldsymbol{N}$

$$v_i = \sum_{I=1}^{n} N_I(X) \bar{v}_{iI} \quad , \quad w_i = \sum_{I=1}^{n} N_I(X) \bar{w}_{iI} \tag{2.9}$$

where, assuming the use of simplicial elements, $n = 3/4$ for 2D/3D problems is the number of the nodes of the element, $\bar{(\cdot)}$ denotes a nodal value, the capital subscript specifies the node and the lower case subscript represents the cartesian direction. In this work, linear shape functions have been used for N_I.

Since Eq. (2.9) must hold for all the test functions in the interpolation space, introducing the spatial discretization (2.9) into Eq. (2.8), the spatial semi-discretized form of the momentum equations in the UL framework for the node I reads

$$\underbrace{\int_\Omega N_I \rho d\Omega\ \dot{v}_i}_{f_{Ii}^{dyn}} + \underbrace{\int_\Omega \frac{\partial N_I}{\partial x_j} \sigma_{ij} d\Omega}_{f_{Ii}^{int}} = \underbrace{\int_\Omega N_I b_i d\Omega + \int_{\Gamma_t} N_I t_i^p d\Gamma}_{f_{Ii}^{ext}} \tag{2.10}$$

where $\boldsymbol{f}^{dyn}$, $\boldsymbol{f}^{int}$ and $\boldsymbol{f}^{ext}$ are the dynamic, internal and external forces, respectively, expressed in the UL framework.

For convenience, the semi-discretized form of the momentum equations in the total Lagrangian (TL) framework is also presented here. This is written as [1]

$$\underbrace{\int_{\Omega_0} N_I \rho_0 d\Omega \, \dot{v}_i}_{{}^{TL}f_{Ii}^{dyn}} + \underbrace{\int_{\Omega_0} \frac{\partial N_I}{\partial X_j} P_{ij} d\Omega}_{{}^{TL}f_{Ii}^{int}} = \underbrace{\int_{\Omega_0} N_I b_i d\Omega + \int_{\Gamma_0} N_I t_{0i}^p d\Gamma}_{{}^{TL}f_{Ii}^{ext}} \tag{2.11}$$

where $\boldsymbol{P}$ is the first Piola–Kirchhoff stress tensor, or the nominal stress tensor, and ${}^{TL}\boldsymbol{f}^{dyn}$, ${}^{TL}\boldsymbol{f}^{int}$ and ${}^{TL}\boldsymbol{f}^{ext}$ are the dynamic, internal and external forces, respectively, expressed in the TL framework. All the variables with vectors subscript $(\cdot)_0$ refer to the last known configuration. Note that Eq. (2.11) can be obtained from Eq. (2.10) by pull back transformations on all its terms [1].

For the sake of clarity in the notation, the terms referred to the TL description are denoted with the left index ${}^{TL}(\cdot)$. Unless otherwise specified, the variables belong to the UL description.

2.1.2 Time Integration

In this work, the kinematic variables have been integrated in time using a second order scheme. In particular, the implicit Newmark's integration rule has been adopted. For the general case, this rule states that accelerations and displacements are computed as

$$\begin{aligned} {}^{n+1}\dot{\boldsymbol{v}} &= \frac{1}{\gamma \Delta t}\left({}^{n+1}\boldsymbol{v} - {}^{n}\boldsymbol{v}\right) - \frac{1-\gamma}{\gamma}{}^{n}\dot{\boldsymbol{v}} \\ {}^{n+1}\boldsymbol{u} &= {}^{n}\boldsymbol{u} + \Delta t \frac{\gamma-\beta}{\gamma}{}^{n}\boldsymbol{v} + \Delta t \frac{\beta}{\gamma}{}^{n+1}\boldsymbol{v} + \Delta t^2 \frac{\gamma - 2\beta}{2\gamma}{}^{n}\dot{\boldsymbol{v}} \end{aligned} \tag{2.12}$$

where β and γ are the so-called Newmark's parameters [1]. This time integration scheme is unconditionally stable if the following relation holds

$$\gamma \geq 2\beta \geq \frac{1}{2} \tag{2.13}$$

In the present work, the Newmark's parameters chosen are $\beta = \frac{1}{4}$ and $\gamma = \frac{1}{2}$.

Replacing the numerical values of the constants in Eq. (2.12) yields

$${}^{n+1}\dot{\boldsymbol{v}} = \frac{2}{\Delta t}\left({}^{n+1}\boldsymbol{v} - {}^{n}\boldsymbol{v}\right) - {}^{n}\dot{\boldsymbol{v}} \tag{2.14}$$

$${}^{n+1}\boldsymbol{u} = {}^{n}\boldsymbol{u} + \frac{\Delta t}{2}\left({}^{n+1}\boldsymbol{v} + {}^{n}\boldsymbol{v}\right) \tag{2.15}$$

2.1.3 Linearization

Although the problem is set out in the UL framework, the linearization for the velocities increment of the momentum equations is performed first on the TL semi-discretized form (2.11). The UL linearized form is obtained by performing a push-forward transformation on the TL form. This is justified by the easier derivation of the tangent matrix in the TL framework. In fact, in Eq. (2.11) the only variable that depends on time is the nominal stress $\boldsymbol{P}$, while in the UL form (2.10) the time-dependent variables are the updated domain Ω, the Cauchy stress tensor $\boldsymbol{\sigma}$ and the spatial derivatives $\boldsymbol{\partial N / \partial x}$. For the sake of clarity, the linearization of the internal and dynamic forces will be performed separately.

Internal Component of the Tangent Matrix

From Eq. (2.11) the internal forces in the TL description are defined as

$$ {}^{TL} f_{Ii}^{int} = \int_{\Omega_0} \frac{\partial N_I}{\partial X_j} P_{ij} d\Omega_0 \tag{2.16} $$

The constitutive relation is expressed in rate form. Hence it is more convenient to perform the linearization of the material derivative of the internal forces and then integrate for the time step increment Δt. The material time derivative of (2.16) is

$$ {}^{TL} \dot{f}_{Ii}^{int} = \int_{\Omega_0} \frac{\partial N_I}{\partial X_j} \dot{P}_{ij} d\Omega_0 \tag{2.17} $$

The infinitesimal increment of Eq. (2.17) is

$$ {}^{TL} \delta \dot{f}_{Ii}^{int} = \int_{\Omega_0} \frac{\partial N_I}{\partial X_j} \delta \dot{P}_{ij} d\Omega_0 \tag{2.18} $$

The first Piola–Kirchhoff stress tensor $\boldsymbol{P}$ is not typically used because it is not symmetric and its rate is a non-objective measure. For these reasons, in the TL framework it is more convenient to work with the second Piola–Kirchhoff stress tensor $\boldsymbol{S}$ and its rate. These stress rate measures are related each other through the following relation

$$ \dot{P}_{ij} = \dot{S}_{ir} F_{rj}^T + S_{ir} \dot{F}_{rj}^T \tag{2.19} $$

where $\boldsymbol{F}$ is the deformation gradient tensor defined as

$$ F_{ij} = \frac{\partial x_i}{\partial X_j} \tag{2.20} $$

Substituting Eq. (2.19) into (2.18) yields

$$ {}^{TL}\delta \dot{f}_{Ii}^{int} = \underbrace{\int_{\Omega_0} \frac{\partial N_I}{\partial X_j} F_{ir} \delta \dot{S}_{jr} d\Omega_0}_{{}^{TL}\delta \dot{f}_{Ii}^{m}} + \underbrace{\int_{\Omega_0} \frac{\partial N_I}{\partial X_j} S_{jr} \delta \dot{F}_{ir}^{T} d\Omega_0}_{{}^{TL}\delta \dot{f}_{Ii}^{g}} \tag{2.21} $$

Equation (2.21) shows that the increment of the material time derivative of the internal forces can be split into material and geometric parts, ${}^{TL}\delta \dot{\boldsymbol{f}}^{m}$ and ${}^{TL}\delta \dot{\boldsymbol{f}}^{g}$, respectively. The former accounts for the material response through the rate of the second Piola–Kirchhoff stress tensor and the second term is the initial stress term that contains the information of the updated stress field. Note that, up to now, no constitutive relationships have been introduced and the above derivation holds for a general continuum.

Material Tangent Matrix

From Eq. (2.21), the material part of the material time derivative of the internal forces reads

$$ {}^{TL}\delta \dot{f}_{Ii}^{m} = \int_{\Omega_0} \frac{\partial N_I}{\partial X_j} F_{ir} \delta \dot{S}_{jr} d\Omega_0 \tag{2.22} $$

For the derivation of the material tangent matrix, the constitutive relation between the stress and the strain measures is required. In order to maintain the formulation as general as possible, the stress rate measure is related to the deformation rate through a tangent constitutive tensor, as

$$ \dot{S}_{ij} = C_{ijkl} \dot{E}_{kl} \tag{2.23} $$

where $\boldsymbol{C}$ is a fourth-order tensor and $\boldsymbol{E}$ is the Green–Lagrange strain tensor. Equation (2.23) can also be expressed in Voigt notation as

$$ \{\dot{\boldsymbol{S}}\} = [\boldsymbol{C}]\{\dot{\boldsymbol{E}}\} \tag{2.24} $$

where $\{(\cdot)\}$ denotes a vector with components $[(\cdot)_{11}, (\cdot)_{22}, (\cdot)_{33}, (\cdot)_{12}, (\cdot)_{13}, (\cdot)_{23}]$. As it will be shown in the following sections, Eq. (2.23) can represent both a Kirchhoff solid material and a Newtonian fluid. If different constitutive laws are used, Eq. (2.23) should be modified accordingly in order to derive the material part of the tangent matrix.

Using the Voigt notation, the Green–Lagrange strain tensor can be expressed in terms of the nodal velocities as

$$ \{\dot{\boldsymbol{E}}\} = \boldsymbol{B_0}\bar{\boldsymbol{v}} \tag{2.25} $$

where for a plane strain problem

$$\boldsymbol{B}_0 = \begin{bmatrix} \dfrac{\partial N_I}{\partial X}\dfrac{\partial x}{\partial X} & \dfrac{\partial N_I}{\partial X}\dfrac{\partial y}{\partial X} \\ \dfrac{\partial N_I}{\partial Y}\dfrac{\partial x}{\partial Y} & \dfrac{\partial N_I}{\partial Y}\dfrac{\partial y}{\partial Y} \\ \dfrac{\partial N_I}{\partial X}\dfrac{\partial x}{\partial Y} + \dfrac{\partial N_I}{\partial Y}\dfrac{\partial x}{\partial X} & \dfrac{\partial N_I}{\partial X}\dfrac{\partial y}{\partial Y} + \dfrac{\partial N_I}{\partial Y}\dfrac{\partial y}{\partial X} \end{bmatrix} \tag{2.26}$$

Substituting Eq. (2.25) in (2.24)

$$\{\dot{\boldsymbol{S}}\} = [\boldsymbol{C}]\,\boldsymbol{B_0 v} \tag{2.27}$$

Substituting Eq. (2.27) into (2.22) yields

$${}^{TL}\delta\dot{\boldsymbol{f}}^m = \int_{\Omega_0} \boldsymbol{B}_0^T\,[\boldsymbol{C}]\,\boldsymbol{B}_0 d\Omega_0 \delta\bar{\boldsymbol{v}} \tag{2.28}$$

In order to obtain the increment of the internal forces, the material time derivative of the internal forces increment is integrated over a time step increment Δt as

$${}^{TL}\delta\boldsymbol{f}^m = {}^{TL}\delta\dot{\boldsymbol{f}}^m \Delta t \tag{2.29}$$

From Eqs. (2.29) and (2.28)

$${}^{TL}\delta\boldsymbol{f}^m = \int_{\Omega_0} \boldsymbol{B}_0^T \Delta t\,[\boldsymbol{C}]\,\boldsymbol{B}_0 d\Omega_0 \delta\bar{\boldsymbol{v}} \tag{2.30}$$

From Eq. (2.30), the material tangent matrix in the TL description can be computed as

$${}^{TL}\boldsymbol{K}^m = \int_{\Omega_0} \boldsymbol{B}_0^T \Delta t\,[\boldsymbol{C}]\,\boldsymbol{B}_0 d\Omega_0 \tag{2.31}$$

The material tangent matrix for the UL framework is obtained by applying a push-forward transformation on each term of Eq. (2.31) and integrating over the updated domain Ω. The following relations hold

$$d\Omega_0 = \frac{d\Omega}{J} \tag{2.32}$$

$$\frac{\partial N_I}{\partial X_j} = \frac{\partial N_I}{\partial x_k} F_{kj} \tag{2.33}$$

$$C_{ijkl} = F_{mi}^{-1} F_{nj}^{-1} F_{ok}^{-1} F_{pl}^{-1} c_{mnop}^{\tau} = F_{mi}^{-1} F_{nj}^{-1} F_{ok}^{-1} F_{pl}^{-1} c_{mnop}^{\sigma} J \tag{2.34}$$

where c^{τ} is the tangent moduli corresponding to the material time derivative of the Kirchhoff stress tensor $\boldsymbol{\tau}^{\nabla}$ and c^{σ} is the tangent moduli for the rate of the Cauchy stress $\boldsymbol{\sigma}^{\nabla}$. The rate of the Cauchy stress tensor is related to the rate of deformation $\boldsymbol{d}$ through the fourth-order tensor $\boldsymbol{c}^{\sigma}$ by the following expression

$$\boldsymbol{\sigma}^{\nabla} = \boldsymbol{c}^{\sigma} : \boldsymbol{d} \tag{2.35}$$

Substituting Eqs. (2.32)–(2.34) into (2.31) and using the minor symmetries, the material tangent matrix for the UL reads

$$\boldsymbol{K}^{m}_{IJ} = \int_{\Omega^e} \boldsymbol{B}^{T}_{I} \Delta t \left[\boldsymbol{c}^{\sigma}\right] \boldsymbol{B}_{J} d\Omega \tag{2.36}$$

For the node I of a 3D element, matrix $\boldsymbol{B}$ is

$$\boldsymbol{B}_{I} = \begin{bmatrix} \dfrac{\partial N_I}{\partial x} & 0 & 0 \\ 0 & \dfrac{\partial N_I}{\partial y} & 0 \\ 0 & 0 & \dfrac{\partial N_I}{\partial z} \\ \dfrac{\partial N_I}{\partial y} & \dfrac{\partial N_I}{\partial x} & 0 \\ \dfrac{\partial N_I}{\partial z} & 0 & \dfrac{\partial N_I}{\partial x} \\ 0 & \dfrac{\partial N_I}{\partial z} & \dfrac{\partial N_I}{\partial y} \end{bmatrix} \tag{2.37}$$

Geometric Tangent Matrix

The geometric tangent matrix for the UL framework is derived next using the same procedure adopted for the material components. Hence, first the linearization is performed using the TL form and then the UL tangent matrix is obtained by performing the required transformation over the TL terms.

From Eq. (2.21)

$${}^{TL}\delta \dot{f}^{g}_{Ii} = \int_{\Omega_0} \frac{\partial N_I}{\partial X_j} S_{jr} \delta \dot{F}^{T}_{ir} d\Omega_0 \tag{2.38}$$

where the rate of the deformation gradient is defined as

$$\dot{F}_{ij} = \frac{\partial N_J}{\partial X_j} \bar{v}_{Ji} \tag{2.39}$$

Substituting Eq. (2.39) into (2.38), the geometric components of the internal power in the TL description can be written as

$$^{TL}\delta \dot{f}^g_{Ii} = \int_{\Omega_0} \frac{\partial N_I}{\partial X_j} S_{jr} \frac{\partial N_J}{\partial X_r} d\Omega_0 \; \delta \bar{v}_{Ji} \tag{2.40}$$

Integrating Eq. (2.40) on time for a time step increment Δt yields

$$^{TL}\delta f^g_{Ii} = \int_{\Omega_0} \frac{\partial N_I}{\partial X_j} \Delta t S_{jr} \frac{\partial N_J}{\partial X_r} d\Omega \; \delta_{ik} \delta \bar{v}_{Jk} \tag{2.41}$$

In order to recover the UL form, the Piola identity has to be recalled, i.e.

$$\boldsymbol{S} = \boldsymbol{F}^{-1} \boldsymbol{\sigma} \boldsymbol{F}^{-T} \boldsymbol{J} \tag{2.42}$$

The geometric tangent matrix in the UL framework is obtained by substituting Eqs. (2.32), (2.33) and (2.42) into (2.41) and using the symmetries. This leads to

$$K^g_{IJik} = \int_{\Omega} \frac{\partial N_I}{\partial x_j} \Delta t \sigma_{jr} \frac{\partial N_J}{\partial x_r} d\Omega \delta_{ik} \tag{2.43}$$

or also

$$\boldsymbol{K}^g_{IJ} = \boldsymbol{I} \int_{\Omega} \boldsymbol{\beta}^T_I \Delta t \boldsymbol{\sigma} \boldsymbol{\beta}_J d\Omega \tag{2.44}$$

where $\boldsymbol{I}$ is the second order identity tensor and matrix $\boldsymbol{\beta}$ for 3D problems is

$$\boldsymbol{\beta}_I = \left[\frac{\partial N_I}{\partial x} \; \frac{\partial N_I}{\partial y} \; \frac{\partial N_I}{\partial z} \right]^T \tag{2.45}$$

Dynamic Component of the Tangent Matrix

The dynamic component of the tangent matrix in the UL description can be derived directly from the UL dynamic term f^{dyn}_{Ii} of Eq. (2.10). This reads

$$f^{dyn}_{Ii} = \int_{\Omega} N_I \rho d\Omega \; \dot{v}_i \tag{2.46}$$

Equation (2.46) has to be discretized in time with the purpose of replacing the accelerations by the velocities using the time integration scheme described in Eq. (2.14).

Introducing Eq. (2.14) into (2.46) and differentiating for the increment of velocities, the dynamic components of the tangent matrix are obtained as

$$K^{\rho}_{IJij} = \delta_{ij} \int_{\Omega} N_I \frac{2\rho}{\Delta t} N_J d\Omega \tag{2.47}$$

Or also

$$\boldsymbol{K}^{\rho}_{IJ} = \boldsymbol{I} \int_{\Omega} N_I \frac{2\rho}{\Delta t} N_J d\Omega \tag{2.48}$$

2.1.4 Incremental Solution Scheme

The problem is solved through an implicit iterative scheme. At each iteration i the velocity increments are computed as

$$\boldsymbol{K}^i \boldsymbol{\Delta \bar{v}} = \boldsymbol{R}^i ({}^{n+1}\bar{\boldsymbol{v}}^i, {}^{n+1}\boldsymbol{\sigma}^i) \tag{2.49}$$

where $\boldsymbol{K}$ is the tangent matrix computed as the sum of the internal, the geometric and the dynamic components, given by Eqs. (2.36), (2.44) and (2.48) respectively, as

$$\boldsymbol{K} = \boldsymbol{K}^m + \boldsymbol{K}^g + \boldsymbol{K}^{\rho} \tag{2.50}$$

$\boldsymbol{R}$ is the residual and it is computed from Eq. (2.10) as

$$\begin{aligned} {}^{n+1}R_{Ii} = \int_{\Omega} N_I \rho N_J d\Omega \, {}^{n+1}\dot{\bar{v}}_{Ji} + \int_{\Omega} \frac{\partial N_I}{\partial x_j} {}^{n+1}\sigma_{ij} d\Omega - \int_{\Omega} N_I \, {}^{n+1}b_i d\Omega + \\ - \int_{\Gamma_t} N_I \, {}^{n+1}t_i^p d\Gamma \end{aligned} \tag{2.51}$$

In Eq. (2.51) ${}^{n+1}R_{Ii}$ is the residual of the momentum equations referred to node I and the cartesian direction i. Note that the Cauchy stress tensor still appears in its 'continuum' form because up to now it has not been written as a function of the nodal unknowns. This is done for keeping the generality of the formulation. Only after the introduction of the constitutive laws, it will be possible to compute the Cauchy stress tensor as a function of the nodal unknowns.

In Box 1 the iterative solution incremental scheme of the velocity formulation for a generic time interval $[{}^{n}t, {}^{n+1}t]$ of duration Δt is described.

For each iteration i within a time interval:

1. Compute the nodal velocity increments $\boldsymbol{\Delta}\bar{\boldsymbol{v}}$:

$$\boldsymbol{K}^i \boldsymbol{\Delta}\bar{\boldsymbol{v}} = \boldsymbol{R}^i({}^{n+1}\bar{\boldsymbol{v}}^i, \boldsymbol{\sigma}({}^{n+1}\bar{\boldsymbol{v}}^i))$$

where: $\boldsymbol{K}^i = \boldsymbol{K}^m({}^{n+1}\bar{\boldsymbol{x}}^i, \boldsymbol{c}^{\sigma,i}) + \boldsymbol{K}^g\left({}^{n+1}\bar{\boldsymbol{x}}^i, \boldsymbol{\sigma}(\bar{\boldsymbol{v}}^i)\right) + \boldsymbol{K}^\rho({}^{n+1}\bar{\boldsymbol{x}}^i)$

2. Update the nodal velocities: ${}^{n+1}\bar{\boldsymbol{v}}^{i+1} = {}^{n+1}\bar{\boldsymbol{v}}^i + \boldsymbol{\Delta}\bar{\boldsymbol{v}}$

3. Update the nodal coordinates: ${}^{n+1}\bar{\boldsymbol{x}}^{i+1} = {}^{n+1}\bar{\boldsymbol{x}}^i + \bar{\boldsymbol{u}}(\boldsymbol{\Delta}\bar{\boldsymbol{v}})$

4. Compute the updated stress tensors: $\boldsymbol{\sigma}({}^{n+1}\bar{\boldsymbol{v}}^{i+1})$ and $\boldsymbol{\sigma}^\nabla({}^{i+1}\bar{\boldsymbol{v}}^{i+1})$

5. Check convergence: $\| {}^{n+1}\boldsymbol{R}^{i+1}({}^{n+1}\bar{\boldsymbol{v}}^{i+1}) \| < tolerance$

If condition 5 is not fulfilled, return to 1 with $i \leftarrow i + 1$.

Box 1. Iterative incremental solution scheme for the velocity formulation

2.2 Mixed Velocity–Pressure Formulation

In this work, the mixed Velocity–Pressure formulation is derived as an extension of the Velocity formulation presented in the previous section. The governing equations are the linear momentum equations and the linear relation between the time variation of pressure and the volumetric strain rate.

The problem is solved using a two-step Gauss–Seidel partitioned iterative scheme. First the momentum equations are solved in terms of velocity increments and including the (known) pressures at the previous iteration in the residual expression. Then the continuity equation is solved for the pressure using the updated velocities computed from the momentum equations. It will be shown that using this not intrusive scheme, it is possible to take advantage of most of the velocity formulation derived in the previous section. In particular, the incremental velocity scheme for the momentum equations (Box 1) and the structure of the tangent matrix (2.50) hold also for the mixed Velocity–Pressure formulation. The same linear interpolation has been used for the velocity and the pressure fields. It is well known that, for incompressible (or quasi-incompressible) problems, this combination does not fulfill the *inf–sup* condition [3] and a stabilization method is required. However, as mentioned in the section devoted to the velocity formulation, the aim of this part is to keep the formulation as general as possible without referring to a specific material. Hence only in

the next chapter, when the mixed Velocity–Pressure formulation is used for solving quasi-incompressible problems, the required stabilization will be introduced in the scheme.

2.2.1 Quasi-incompressible Form of the Continuity Equation

Mixed formulations are often used for dealing with incompressible materials. In these problems it is useful to write the stress and the strain measures as the sum of deviatoric and hydrostatic, or volumetric, parts. Hence the Cauchy stress tensor is decomposed as

$$\sigma_{ij} = \sigma'_{ij} + \sigma^h \delta_{ij} \tag{2.52}$$

with

$$\sigma^h = \frac{\sigma_{kk}}{3} \tag{2.53}$$

where $\boldsymbol{\sigma}'$ and $\sigma^h \boldsymbol{I}$ are the deviatoric and the hydrostatic parts of the Cauchy stress tensor, respectively. The pressure p is defined positive in the tensile state and equal to the hydrostatic parts of the Cauchy stress tensor σ^h. Hence

$$p := \sigma^h \tag{2.54}$$

The Cauchy stress tensor can be computed as

$$\sigma_{ij} = \sigma'_{ij} + p\delta_{ij} \tag{2.55}$$

The same decomposition is done for the spatial strain rate tensor $\boldsymbol{d}$. So

$$d_{ij} = d'_{ij} + d^h \delta_{ij} \tag{2.56}$$

with

$$d^h = \frac{d_{kk}}{3} \tag{2.57}$$

where $\boldsymbol{d}'$ and $d^h \boldsymbol{I}$ are the deviatoric and the hydrostatic parts of the strain rate tensor, respectively. The strain rate tensor is computed from the velocities as

$$d_{ij} = \frac{1}{2}\left(\frac{\partial v_i}{\partial x_j} + \frac{\partial v_j}{\partial x_i}\right) \tag{2.58}$$

The volumetric strain rate is defined from Eqs. (2.57) and (2.58) as

$$d^v = d_{kk} = \frac{\partial v_k}{\partial x_k} \tag{2.59}$$

The closure equation for the mixed Velocity–Pressure formulation is the linear relation between the change in time of the pressure and the volumetric strain rate. This reads as

$$\frac{1}{\kappa}\frac{\partial p}{\partial t} = d^v \tag{2.60}$$

where κ is a parameter that depends on the constitutive equation. Typically κ is the bulk modulus of the material.

In conclusion, the local form of the whole problem for the mixed Velocity–Pressure formulation is formed by the linear momentum equations (Eq. (2.1)) and the pressure-strain rate relation given by Eq. (2.60). The linear momentum equations have been already discretized and linearized for the increments of velocities in the previous section devoted to the Velocity formulation. That form holds also for the mixed formulation. So, in the following, only the discretization of Eq. (2.60) is given. This equation is a restriction on the generality of the constitutive laws that can be analyzed with the mixed Velocity–Pressure formulation. It will be shown that the constitutive models for hypoelastic solids and quasi-incompressible Newtonian fluids fulfill this relation. In fluid dynamics, Eq. (2.60) represents the *continuity*, or *mass balance*, equation for quasi-incompressible fluids. In fact, Eq. (2.60) with $\kappa = \infty$ is the canonical form of the continuity equation of the Navier–Stokes problem. For this reason, from here on Eq. (2.60) will be called 'continuity equation'.

Multiplying Eq. (2.60) by arbitrary test functions q (with dimensions of pressure), integrating over the analysis domain Ω and bringing all the terms at the left hand side gives

$$\int_\Omega \frac{q}{\kappa}\frac{\partial p}{\partial t} d\Omega - \int_\Omega q d^v d\Omega = 0 \tag{2.61}$$

Both the trial and the test functions for the pressure are interpolated in space using the same shape functions $\boldsymbol{N}$.

$$p = \sum_{I=1}^{n} N_I \bar{p}_I \quad , \quad q = \sum_{I=1}^{n} N_I \bar{q}_I \tag{2.62}$$

where $n = 3/4$ for 2D/3D problems is the number of the nodes of the simplex. In this work, linear shape functions have been used for N_I, as for the velocity.

Combining Eq. (2.62) with (2.61) and solving for all the admissible test functions q, yields

$$\int_\Omega N_I \frac{1}{\kappa} N_J d\Omega \dot{\bar{p}}_J - \int_\Omega N_I \frac{\partial N_J}{\partial x_i} d\Omega \bar{v}_{iJ} = 0 \tag{2.63}$$

Regarding the time integration a first order scheme has been adopted for the pressure. Hence, for a time interval $[{}^n t, {}^{n+1} t]$ of duration Δt the first and the second variations in time of the pressure are computed as

$$ {}^{n+1}\dot{\boldsymbol{p}} = \frac{{}^{n+1}\boldsymbol{p} - {}^{n}\boldsymbol{p}}{\Delta t} \tag{2.64} $$

$$ {}^{n+1}\ddot{\boldsymbol{p}} = \frac{{}^{n+1}\boldsymbol{p} - {}^{n}\boldsymbol{p}}{\Delta t^2} - \frac{{}^{n}\dot{\boldsymbol{p}}}{\Delta t} \tag{2.65} $$

Introducing Eq. (2.64) in Eq. (2.63), the discretized form of the continuity equation is

$$ -\boldsymbol{Q}^{T\,n+1}\bar{\boldsymbol{v}} + \frac{1}{\Delta t}\boldsymbol{M}_1{}^{n+1}\bar{\boldsymbol{p}} = {}^{n}\boldsymbol{g} \tag{2.66} $$

where

$$ M_{1_{IJ}} = \int_{\Omega^e} N_I \frac{1}{\kappa} N_J d\Omega \tag{2.67} $$

$$ \boldsymbol{Q}_{IJ} = \int_{\Omega^e} \boldsymbol{B}_I^T \boldsymbol{m} N_J d\Omega \tag{2.68} $$

$$ {}^{n}g_I = \int_{\Omega^n} N_I \frac{1}{\kappa \Delta t} N_J d\Omega \, {}^{n}\bar{p}_J \tag{2.69} $$

where $\boldsymbol{B}$ has been defined in Eq. (2.37) and $\boldsymbol{m}= [1, 1, 1, 0, 0, 0]^T$.

2.2.2 Solution Method

In the mixed Velocity–Pressure formulation the problem is solved through a partitioned iterative scheme. Specifically, the linear momentum equations are solved for the velocity increments as in the Velocity formulation. On the other hand, the continuity equation is solved for the pressure in the updated configuration using the velocity field computed with the linear momentum equations. In order to guarantee the coupling between the continuity equation and the linear momentum equations (or equally between the pressure and the velocities) the pressure must appear in the right hand side of the linear momentum equations. For this purpose the Cauchy stress tensor must be computed as the sum of its deviatoric part and the pressure, as Eq. (2.55). Otherwise, the Velocity–Pressure formulation would be uncoupled and totally equivalent to the Velocity formulation.

In conclusion, for a general time interval $[{}^{n}t, {}^{n+1}t]$ of duration Δt the following linear systems are solved for each iteration i

$$ \boldsymbol{K}^i \Delta\bar{\boldsymbol{v}} = \boldsymbol{R}^i({}^{n+1}\bar{\boldsymbol{v}}^i, {}^{n+1}\boldsymbol{\sigma}'^i, {}^{n+1}\boldsymbol{p}^i) \tag{2.70} $$

$$ \frac{1}{\Delta t}\boldsymbol{M}_1{}^{n+1}\bar{\boldsymbol{p}}^{i+1} = \boldsymbol{Q}^{T\,n+1}\bar{\boldsymbol{v}}^{i+1} + {}^{n}\boldsymbol{g}^{n}\bar{\boldsymbol{p}}^i \tag{2.71} $$

where $\boldsymbol{K}$ is the same tangent matrix as for the Velocity formulation (Eq. (2.50)) and the residual $\boldsymbol{R}$ is computed using the pressure of the previous iteration and the deviatoric part of the Cauchy stress as

$$
\begin{aligned}
{}^{n+1}R_{Ii} = \int_{\Omega} N_I \rho N_J d\Omega \, {}^{n+1}\bar{\dot{v}}_{Ji} + \int_{\Omega} \frac{\partial N_I}{\partial x_j} {}^{n+1}\sigma'_{ij} d\Omega + \\
+ \int_{\Omega} \frac{\partial N_I}{\partial x_j} \delta_{ij} N_J d\Omega \, {}^{n+1}\bar{p}_J - \int_{\Omega} N_I \, {}^{n+1}b_i d\Omega - \int_{\Gamma_t} N_I \, {}^{n+1}t_i^p d\Gamma
\end{aligned}
\tag{2.72}
$$

In Box 2, the iterative incremental solution scheme for a generic continuum via the mixed Velocity–Pressure formulation is shown for a time interval $[{}^{n}t, {}^{n+1}t]$.

For each iteration i within a time interval:

1. Compute the nodal velocity increments $\boldsymbol{\Delta}\bar{\boldsymbol{v}}$:

$$\boldsymbol{K}^i \boldsymbol{\Delta}\bar{\boldsymbol{v}} = \boldsymbol{R}^i({}^{n+1}\bar{\boldsymbol{v}}^i, {}^{n+1}\bar{\boldsymbol{p}}^i)$$

where: $\boldsymbol{K}^i = \boldsymbol{K}^m({}^{n+1}\bar{\boldsymbol{x}}^i, \boldsymbol{c}^{\sigma,i}) + \boldsymbol{K}^g\left({}^{n+1}\bar{\boldsymbol{x}}^i, \boldsymbol{\sigma}^i(\bar{\boldsymbol{v}}^i, \bar{\boldsymbol{p}}^i)\right) + \boldsymbol{K}^\rho({}^{n+1}\bar{\boldsymbol{x}}^i)$

2. Update the nodal velocities: ${}^{n+1}\bar{\boldsymbol{v}}^{i+1} = {}^{n+1}\bar{\boldsymbol{v}}^i + \boldsymbol{\Delta}\bar{\boldsymbol{v}}$

3. Update the nodal coordinates: ${}^{n+1}\bar{\boldsymbol{x}}^{i+1} = {}^{n+1}\bar{\boldsymbol{x}}^i + \bar{\boldsymbol{u}}(\boldsymbol{\Delta}\bar{\boldsymbol{v}})$

4. Compute the nodal pressures ${}^{n+1}\bar{\boldsymbol{p}}^{i+1}$:

$$\frac{1}{\Delta t}\boldsymbol{M}_1 \, {}^{n+1}\bar{\boldsymbol{p}}^{i+1} = \boldsymbol{Q}^T \, {}^{n+1}\bar{\boldsymbol{v}}^{i+1} + \boldsymbol{g}^n({}^{n}\bar{\boldsymbol{p}}^i)$$

5. Compute the updated stress measures:

$${}^{n+1}\boldsymbol{\sigma}^{i+1} = {}^{n+1}\boldsymbol{\sigma}'(\bar{\boldsymbol{v}}^{i+1}) - {}^{n+1}p^{i+1}\boldsymbol{I}$$

6. Check convergence: $\| \, {}^{n+1}\boldsymbol{R}^{i+1}({}^{n+1}\bar{\boldsymbol{v}}^{i+1}, {}^{n+1}\bar{\boldsymbol{p}}^{i+1}) \, \| < tolerance$

If condition 6 is not fulfilled, return to 1 with $i \leftarrow i + 1$.

Box 2. Iterative solution scheme for a generic continuum using the mixed Velocity–Pressure formulation

2.3 Hypoelasticity

Using the definition of Truesdell [4], a hypoelastic body is a material which may soften or harden in strain but in general has neither preferred state nor preferred stress. The hypoelastic laws were created with the purpose of transferring the linear theory of elasticity from the small to the finite strains regime [4]. In [5] a deep dissertation about the differences between elasticity and hypoelasticity is given.

A hypoelastic body is defined by the constitutive equation [6]

$$rate\ of\ stress = f(rate\ of\ deformation) \tag{2.73}$$

In the rate theory it is crucial to guarantee the *objectivity* and the *frame-invariance*, or *frame-indifference*, of the scheme. A material is frame invariant if its properties do not depend on the change of observer. An objective constitutive equation is defined to be invariant for all changes of the observer [7]. For guaranteeing the frame indifference, the constitutive law has to be isotropic [8]. This represents a constraint for hypoelastic models. This limitation is even more severe if also plasticity is included in the model. In fact, for hypoelastic–plastic materials, also the yield condition is required to be isotropic [9].

The stress rate cannot be computed simply as a material derivative because it leads to a non-objective measure of stress [1]. In particular, rigid rotations may originate a wrong state of stress if the stress rate is computed as the material time derivative of the Cauchy stress [1]. However, many objective measures of rate of stress are available. The most common ones are the Truesdell's and Jaumann's Cauchy stress rate measures. From here on, an objective rate measure will be denoted by the upper inverse triangle index $(\cdot)^{\triangledown}$.

Most of hypoelastic laws relate linearly the stress rate to the rate of deformation. Hence, Eq. (2.73) is now rewritten in the following form

$$\boldsymbol{\sigma}^{\triangledown} = \boldsymbol{c} : \boldsymbol{d} \tag{2.74}$$

where $\boldsymbol{\sigma}^{\triangledown}$ is the Cauchy stress rate tensor, $\boldsymbol{c}$ is the tangent moduli tensor and $\boldsymbol{d}$ is the deformation rate tensor.

From Eq. (2.74) it can be deduced that this class of hypoelastic materials has a rate-independent and incrementally linear and reversible behavior. So, as for the elastic materials, in the small deformation regime, the strains and the stresses are totally recovered upon the unloading process. Nevertheless, for large deformations the hypoelastic laws do not guarantee that the work done in a closed deformation path is zero [10]. However this error can be considered negligible if the elastic deformations are small with respect to the total deformations [1]. For this reason the hypoelastic laws are often used for describing the elastic part of elastic-plastic materials: the plastic deformations in fact represent usually the largest part of the overall deformations.

The Jaumann measure for the rate of the Kirchhoff stress tensor $\boldsymbol{\tau}^{\nabla J}$ is

$$\boldsymbol{\tau}^{\nabla J} = \boldsymbol{c}^{\tau J} : \boldsymbol{d} \tag{2.75}$$

where the tangent moduli fourth-order tensor $\boldsymbol{c}^{\tau J}$ for the Jaumann measure of the Kirchhoff stress rate is

$$c_{ijkl}^{\tau J} = \lambda \delta_{ij}\delta_{kl} + \mu\left(\delta_{ik}\delta_{jl} + \delta_{il}\delta_{kj}\right) \quad , \quad \boldsymbol{c}^{\tau J} = \lambda \boldsymbol{I} \otimes \boldsymbol{I} + 2\mu \mathbf{I} \tag{2.76}$$

where λ and μ are the Lamé constants and they are computed from the Young modulus E and the Poisson ratio ν as

$$\mu = \frac{E}{2(1+\nu)} \tag{2.77}$$

$$\lambda = \frac{\nu E}{(1+\nu)(1-2\nu)} \tag{2.78}$$

and $\mathbf{I}$ is the fourth-order symmetric identity tensor defined as

$$\mathrm{I}_{ijkl} = \frac{1}{2}\left(\delta_{ik}\delta_{jl} + \delta_{il}\delta_{kj}\right) \tag{2.79}$$

Separating the volumetric from the deviatoric part, yields

$$c_{ijkl}^{\tau J} = \kappa \delta_{ij}\delta_{kl} + \mu\left(\delta_{ik}\delta_{jl} + \delta_{il}\delta_{kj} - \frac{2}{3}\delta_{ij}\delta_{kl}\right) \quad , \quad \boldsymbol{c}^{\tau J} = \kappa \boldsymbol{I} \otimes \boldsymbol{I} + 2\mu \mathbf{I}' \tag{2.80}$$

where κ is the bulk modulus and it is computed from the Lamé parameters as

$$\kappa = \lambda + \frac{2}{3}\mu \tag{2.81}$$

and $\mathbf{I}'$ is the fourth-order tensor computed as

$$\mathbf{I}' = \mathbf{I} - \frac{1}{3}\boldsymbol{I} \otimes \boldsymbol{I} \tag{2.82}$$

The Jaumann stress rate measure is defined as

$$\boldsymbol{\sigma}^{\nabla J} = \boldsymbol{c}^{\sigma J} : \boldsymbol{d} \tag{2.83}$$

where $\boldsymbol{c}^{\sigma J}$ is the Jaumann's tangent moduli tensor.

For a anisotropic material the tangent moduli for the Jaumann rate depends on the stress state and it is related to $\boldsymbol{c}^{\tau J}$ as follows

$$c^{\sigma J}_{ijkl} = \frac{c^{\tau J}_{ijkl}}{J} - \sigma_{il}\delta_{kj} \quad , \quad \boldsymbol{c}^{\sigma J} = \frac{\boldsymbol{c}^{\tau J}}{J} - \boldsymbol{\sigma} \otimes \boldsymbol{I} \tag{2.84}$$

Instead, for isotropic materials, the Jaumann's tangent moduli tensors for the Cauchy stress rate and for the Kirchhoff stress rate are identical [1]. So $\boldsymbol{c}^{\sigma J}$ can be computed as

$$c^{\sigma J}_{ijkl} = \lambda\delta_{ij}\delta_{kl} + \mu\left(\delta_{ik}\delta_{jl} + \delta_{il}\delta_{kj}\right) \quad , \quad \boldsymbol{c}^{\sigma J} = \lambda \boldsymbol{I} \otimes \boldsymbol{I} + 2\mu\mathbf{I} \tag{2.85}$$

or equally

$$c^{\sigma J}_{ijkl} = \kappa\delta_{ij}\delta_{kl} + \mu\left(\delta_{ik}\delta_{jl} + \delta_{il}\delta_{kj} - \frac{2}{3}\delta_{ij}\delta_{kl}\right) \quad , \quad \boldsymbol{c}^{\sigma J} = \kappa \boldsymbol{I} \otimes \boldsymbol{I} + 2\mu\mathbf{I}' \tag{2.86}$$

For a 3D problem tensor $\boldsymbol{c}^{\sigma J}$ is $\boldsymbol{c}^{\sigma J} = \begin{bmatrix} \lambda+2\mu & \lambda & \lambda & 0 & 0 & 0 \\ \lambda & \lambda+2\mu & \lambda & 0 & 0 & 0 \\ \lambda & \lambda & \lambda+2\mu & 0 & 0 & 0 \\ 0 & 0 & 0 & \mu & 0 & 0 \\ 0 & 0 & 0 & 0 & \mu & 0 \\ 0 & 0 & 0 & 0 & 0 & \mu \end{bmatrix}$

or, equally, $\boldsymbol{c}^{\sigma J} = \begin{bmatrix} \kappa+\frac{4}{3}\mu & \kappa-\frac{2}{3}\mu & \kappa-\frac{2}{3}\mu & 0 & 0 & 0 \\ \kappa-\frac{2}{3}\mu & \kappa+\frac{4}{3}\mu & \kappa-\frac{2}{3}\mu & 0 & 0 & 0 \\ \kappa-\frac{2}{3}\mu & \kappa-\frac{2}{3}\mu & \kappa+\frac{4}{3}\mu & 0 & 0 & 0 \\ 0 & 0 & 0 & \mu & 0 & 0 \\ 0 & 0 & 0 & 0 & \mu & 0 \\ 0 & 0 & 0 & 0 & 0 & \mu \end{bmatrix}$

A material is said to be isotropic if its behavior is uniform in all directions, so it has no preferred orientations or directions. Many materials, such as metals and ceramics, can be modeled as isotropic for small strains [1]. From the computational point of view, an isotropic constitutive law is much easier to manage than an anisotropic one and it has a lower computational cost. Isotropic laws are preferred, for example, for their symmetry properties. In fact the anisotropic tangent moduli (Eq. (2.84)) is not symmetric while, the isotropic one (Eq. (2.86)) has both minor and major symmetries, in fact

$$minor\ symmetry \quad \leftrightarrow \quad c^{\sigma J}_{ijkl} = c^{\sigma J}_{jikl} = c^{\sigma J}_{ijlk} \tag{2.87}$$

$$major\ symmetry \quad \leftrightarrow \quad c^{\sigma J}_{ijkl} = c^{\sigma J}_{klij} \tag{2.88}$$

For all these reasons, in this work the isotropic law has been used for the hypoelastic model.

The tangent moduli $\boldsymbol{c}^{\sigma J}$ will be introduced into the material part $\boldsymbol{K}^m$ of the global tangent matrix Eq. (2.36) for the Velocity and the mixed Velocity–Pressure formulations indifferently.

As it has already pointed out, the Cauchy stress rate does not coincide with the material derivative of the Cauchy stress tensor. In fact, the following relation holds between both measures

$$\dot{\boldsymbol{\sigma}} = \boldsymbol{\sigma}^{\nabla J} + \boldsymbol{\Omega} \tag{2.89}$$

where $\boldsymbol{\Omega}$ is a tensor that accounts for the rotations and it is defined as

$$\boldsymbol{\Omega} = \boldsymbol{W} \cdot \boldsymbol{\sigma} + \boldsymbol{\sigma} \cdot \boldsymbol{W}^T \tag{2.90}$$

where $\boldsymbol{W}$ is the spin tensor defined as

$$W_{ij} = \frac{1}{2}\left(L_{ij} - L_{ji}\right) = \frac{1}{2}\left(\frac{\partial v_i}{\partial x_j} - \frac{\partial v_j}{\partial x_i}\right) \tag{2.91}$$

In this work the tensor $\boldsymbol{\Omega}$ is computed at the end of each time step. Discretizing in time Eq. (2.89) for the time step interval $[{}^n t, {}^{n+1} t]$ and expanding the Cauchy stress rate, yields

$$\frac{{}^{n+1}\boldsymbol{\sigma} - {}^{n}\boldsymbol{\sigma}}{\Delta t} = \boldsymbol{c}^{\sigma J} : {}^{n+1}\boldsymbol{d} + {}^{n}\boldsymbol{\Omega} \tag{2.92}$$

$\boldsymbol{\Omega}$ can be viewed as a correction of the Cauchy stress tensor. So it can be related to the Cauchy stress tensor of the previous time step as follows

$${}^{n}\hat{\boldsymbol{\sigma}} = {}^{n}\boldsymbol{\sigma} + {}^{n}\boldsymbol{\Omega}\Delta t \tag{2.93}$$

Replacing Eq. (2.93) in (2.92), yields

$$\frac{{}^{n+1}\boldsymbol{\sigma} - {}^{n}\hat{\boldsymbol{\sigma}}}{\Delta t} = \boldsymbol{c}^{\sigma J} : {}^{n+1}\boldsymbol{d} \tag{2.94}$$

Substituting in Eq. (2.94) the relation for $\boldsymbol{c}^{\sigma J}$ using Eq. (2.86), yields

$$\frac{{}^{n+1}\boldsymbol{\sigma} - {}^{n}\hat{\boldsymbol{\sigma}}}{\Delta t} = \left(\kappa \boldsymbol{I} \otimes \boldsymbol{I} + 2\mu \mathbf{I}'\right) : {}^{n+1}\boldsymbol{d} \tag{2.95}$$

Hence,

$$\frac{{}^{n+1}\boldsymbol{\sigma} - {}^{n}\hat{\boldsymbol{\sigma}}}{\Delta t} = \underbrace{\kappa\,(\boldsymbol{I} \otimes \boldsymbol{I}) : {}^{n+1}\boldsymbol{d}}_{{}^{n+1}\dot{p}} + \underbrace{2\mu \mathbf{I}' : {}^{n+1}\boldsymbol{d}}_{{}^{n+1}\dot{\sigma}'} \tag{2.96}$$

The first and the second terms of the right hand side of Eq. (2.96) represent the increment in the time step of the volumetric and deviatoric parts of the Cauchy stress tensor. From Eq. (2.96) it can be deduced that for isotropic hypoelastic solids described using the Jaumann measure, the following relation holds

$$\dot{p} = \kappa \boldsymbol{d}^v \tag{2.97}$$

Equation (2.97) will be used as the closure equation of the mixed Velocity–Pressure formulation for hypoelastic solids. Note that Eq. (2.97) has the same structure as Eq. (2.60) analyzed in the previous section. From Eq. (2.97) using linear shape functions N and integrating on time the pressure with a first order scheme, the same matrix form of Eq. (2.66) obtained for a general material is obtained.

In conclusion the updated stresses can be computed using the velocities only or both the pressure and the velocities, as follows

$${}^{n+1}\boldsymbol{\sigma} = {}^{n}\hat{\boldsymbol{\sigma}} + \Delta t \left(\kappa \boldsymbol{I} \otimes \boldsymbol{I} + 2\mu \mathbf{I}'\right) : {}^{n+1}\boldsymbol{d} \tag{2.98}$$

$${}^{n+1}\boldsymbol{\sigma} = {}^{n}\hat{\boldsymbol{\sigma}} + {}^{n+1}\Delta p \boldsymbol{I} + 2\Delta t \mu \mathbf{I}' : {}^{n+1}\boldsymbol{d} \tag{2.99}$$

Equations (2.98) and (2.99) will be used for computing the Cauchy stress tensor in the Velocity and mixed Velocity–Pressure formulations, respectively.

2.3.1 Velocity Formulation for Hypoelastic Solids

The solution scheme for hypoelastic solids is the one derived in Sect. 2.1.4 for a general continuum. The only modifications required are the definition of the tangent moduli $\boldsymbol{c}^{\sigma}$ in matrix $\boldsymbol{K}^m$ (Eq. (2.36)) and the computation of the Cauchy stress tensor from the nodal velocities according to the hypoelastic model. This tensor appears in the geometric part of the tangent matrix $\boldsymbol{K}^g$ (Eq. (2.44)) and into the residual $\boldsymbol{R}$ (Eq. (2.51)). The tangent moduli tensor is taken from the Jaumann isotropic description and it is the tensor $\boldsymbol{c}^{\sigma J}$ of Eq. (2.86). Concerning the Cauchy stresses, these are computed with Eq. (2.98). The finite element implemented with this hypoelastic velocity formulation is named V-element.

The iterative solution incremental solution scheme for hypoelastic solids using the velocity formulation for a generic time interval $[{}^{n}t, {}^{n+1}t]$ is given in Box 3.

For each iteration i within a time interval:

1. Compute the nodal velocity increments $\boldsymbol{\Delta\bar{v}}$:

$$\boldsymbol{K}^i \boldsymbol{\Delta\bar{v}} = \boldsymbol{R}^i({}^{n+1}\bar{\boldsymbol{v}}^i, \boldsymbol{\sigma}({}^{n+1}\bar{\boldsymbol{v}}^i))$$

where: $\boldsymbol{K}^i = \boldsymbol{K}^m({}^{n+1}\bar{\boldsymbol{x}}^i, \boldsymbol{c}^{\sigma J}) + \boldsymbol{K}^g\left({}^{n+1}\bar{\boldsymbol{x}}^i, \boldsymbol{\sigma}(\bar{\boldsymbol{v}}^i)\right) + \boldsymbol{K}^\rho({}^{n+1}\bar{\boldsymbol{x}}^i)$

2. Update the nodal velocities: ${}^{n+1}\bar{\boldsymbol{v}}^{i+1} = {}^{n+1}\bar{\boldsymbol{v}}^i + \boldsymbol{\Delta\bar{v}}$

3. Update the nodal coordinates: ${}^{n+1}\bar{\boldsymbol{x}}^{i+1} = {}^{n+1}\bar{\boldsymbol{x}}^i + \bar{\boldsymbol{u}}(\boldsymbol{\Delta\bar{v}})$

4. Compute the updated stress tensors:

$${}^{n+1}\boldsymbol{\sigma}^{\nabla,i+1} = \boldsymbol{c}^{\sigma J} : \boldsymbol{d}\left(\bar{\boldsymbol{v}}^{i+1}\right) \;\rightarrow\; {}^{n+1}\boldsymbol{\sigma}^{i+1} = {}^{n}\hat{\boldsymbol{\sigma}} + \Delta t\, {}^{n+1}\boldsymbol{\sigma}^{\nabla,i+1}$$

5. Check convergence: $\| {}^{n+1}\boldsymbol{R}^{i+1}({}^{n+1}\bar{\boldsymbol{v}}^{i+1}) \| < tolerance$

If condition 5 is not fulfilled, return to 1 with $i \leftarrow i+1$.
At the end of each time step: ${}^{n+1}\hat{\boldsymbol{\sigma}} = {}^{n+1}\boldsymbol{\sigma} + \Delta t\boldsymbol{\Omega}\,({}^{n+1}\bar{\boldsymbol{v}}, {}^{n+1}\boldsymbol{\sigma})$

Box 3. Iterative solution scheme for hypoelastic solids using the velocity formulation

All the matrices and vectors in Box 3 are collected in Box 4

$$\boldsymbol{K}^\rho_{IJ} = \boldsymbol{I}\int_\Omega N_I \frac{2\rho}{\Delta t} N_J d\Omega\,,\;\; \boldsymbol{K}^g_{IJ} = \boldsymbol{I}\int_\Omega \beta_I^T \Delta t\boldsymbol{\sigma}\beta_J d\Omega$$

$$\boldsymbol{K}^m_{IJ} = \int_\Omega \boldsymbol{B}_I^T \Delta t\left[\boldsymbol{c}^{\sigma J}\right]\boldsymbol{B}_J d\Omega$$

$$\boldsymbol{c}^{\sigma J} = \begin{bmatrix} \kappa+\frac{4}{3}\mu & \kappa-\frac{2}{3}\mu & \kappa-\frac{2}{3}\mu & 0 & 0 & 0 \\ \kappa-\frac{2}{3}\mu & \kappa+\frac{4}{3}\mu & \kappa-\frac{2}{3}\mu & 0 & 0 & 0 \\ \kappa-\frac{2}{3}\mu & \kappa-\frac{2}{3}\mu & \kappa+\frac{4}{3}\mu & 0 & 0 & 0 \\ 0 & 0 & 0 & \mu & 0 & 0 \\ 0 & 0 & 0 & 0 & \mu & 0 \\ 0 & 0 & 0 & 0 & 0 & \mu \end{bmatrix}$$

$$R_{Ii} = \int_\Omega N_I \rho N_J d\Omega\, \bar{\dot{v}}_{Ji} + \int_\Omega \frac{\partial N_I}{\partial x_j}\sigma_{ij} d\Omega - \int_\Omega N_I b_i d\Omega - \int_{\Gamma_t} N_I t_i^p d\Gamma$$

where $\kappa = \left(\frac{2\mu}{3} + \lambda\right)$ and λ and μ are the Lamé constants

Box 4. Element form of the matrices and vectors in Box 3

2.3.2 *Mixed Velocity–Pressure Formulation for Hypoelastic Solids*

The solution scheme is like the one presented in Sect. 2.2.2. As already explained, the tangent matrix of the mixed Velocity–Pressure formulation is the same as for the Velocity formulation. However the Cauchy stress tensor is computed from the nodal velocities and the nodal pressures using Eq. (2.99). The governing equations are Eqs. (2.70)–(2.71) particularized with the material parameters of a hypoelastic solid. The finite element implemented with this hypoelastic mixed Velocity–Pressure formulation is called VP-element.

In Box 5, the iterative solution incremental scheme for hypoelastic solids using the mixed Velocity–Pressure formulation is given for a generic time interval $[{}^{n}t, {}^{n+1}t]$.

For each iteration i within a time interval:

1. Compute the nodal velocity increments $\boldsymbol{\Delta}\bar{\boldsymbol{v}}$:

$$\boldsymbol{K}^{i}\,\boldsymbol{\Delta}\bar{\boldsymbol{v}} = \boldsymbol{R}^{i}({}^{n+1}\bar{\boldsymbol{v}}^{i}, {}^{n+1}\bar{\boldsymbol{p}}^{i})$$

where $\boldsymbol{K}^{i} = \boldsymbol{K}^{m}({}^{n+1}\bar{\boldsymbol{x}}^{i}, \boldsymbol{c}^{\sigma J}) + \boldsymbol{K}^{g}({}^{n+1}\bar{\boldsymbol{x}}^{i}, \boldsymbol{\sigma}^{i}(\bar{\boldsymbol{v}}^{i}, \bar{\boldsymbol{p}}^{i})) + \boldsymbol{K}^{\rho}({}^{n+1}\bar{\boldsymbol{x}}^{i})$

2. Update the nodal velocities: ${}^{n+1}\bar{\boldsymbol{v}}^{i+1} = {}^{n+1}\bar{\boldsymbol{v}}^{i} + \boldsymbol{\Delta}\bar{\boldsymbol{v}}$

3. Update the nodal coordinates: ${}^{n+1}\bar{\boldsymbol{x}}^{i+1} = {}^{n+1}\bar{\boldsymbol{x}}^{i} + \bar{\boldsymbol{u}}(\boldsymbol{\Delta}\bar{\boldsymbol{v}})$

4. Compute the nodal pressures ${}^{n+1}\bar{\boldsymbol{p}}^{i+1}$:

$$\frac{1}{\Delta t}\boldsymbol{M}_{1}\,{}^{n+1}\bar{\boldsymbol{p}}^{i+1} = \boldsymbol{Q}^{T}\,{}^{n+1}\bar{\boldsymbol{v}}^{i+1} + \boldsymbol{g}^{n}({}^{n}\bar{\boldsymbol{p}}^{i})$$

5. Compute the updated stress measures:

$${}^{n+1}\boldsymbol{\sigma}^{i+1} = {}^{n}\hat{\boldsymbol{\sigma}} + {}^{n+1}\Delta\bar{p}^{i+1}\boldsymbol{I} + 2\mu\Delta t\left[\mathbf{I}' : \boldsymbol{d}\left(\bar{\boldsymbol{v}}^{i+1}\right)\right]$$

6. Check convergence: $\| {}^{n+1}\boldsymbol{R}^{i+1}({}^{n+1}\boldsymbol{v}^{i+1}, {}^{n+1}\boldsymbol{p}^{i+1}) \| < tolerance$

If condition 6 is not fulfilled, return to 1 with $i \leftarrow i + 1$.

At the end of each time step: ${}^{n+1}\hat{\boldsymbol{\sigma}} = {}^{n+1}\boldsymbol{\sigma} + \Delta t\boldsymbol{\Omega}\,({}^{n+1}\bar{\boldsymbol{v}}, {}^{n+1}\boldsymbol{\sigma})$

Box 5. Iterative solution scheme for hypoelastic solid using mixed Velocity–Pressure formulation

All the matrices and vectors that appear in Box 5 are collected in Box 6

Vectors and matrices for the linear momentum equations

$$\boldsymbol{K}^{\rho}_{IJ} = \boldsymbol{I}\int_{\Omega} N_I \frac{2\rho}{\Delta t} N_J d\Omega \,,\;\; \boldsymbol{K}^{g}_{IJ} = \boldsymbol{I}\int_{\Omega} \boldsymbol{\beta}^T_I \Delta t \boldsymbol{\sigma} \boldsymbol{\beta}_J d\Omega$$

$$\boldsymbol{K}^{m}_{IJ} = \int_{\Omega} \boldsymbol{B}^T_I \Delta t \left[\boldsymbol{c}^{\sigma J}\right] \boldsymbol{B}_J d\Omega$$

$$\boldsymbol{c}^{\sigma J} = \begin{bmatrix} \kappa + \frac{4}{3}\mu & \kappa - \frac{2}{3}\mu & \kappa - \frac{2}{3}\mu & 0 & 0 & 0 \\ \kappa - \frac{2}{3}\mu & \kappa + \frac{4}{3}\mu & \kappa - \frac{2}{3}\mu & 0 & 0 & 0 \\ \kappa - \frac{2}{3}\mu & \kappa - \frac{2}{3}\mu & \kappa + \frac{4}{3}\mu & 0 & 0 & 0 \\ 0 & 0 & 0 & \mu & 0 & 0 \\ 0 & 0 & 0 & 0 & \mu & 0 \\ 0 & 0 & 0 & 0 & 0 & \mu \end{bmatrix}$$

$$R_{Ii} = \int_{\Omega} N_I \rho N_J d\Omega \; \bar{\dot{v}}_{Ji} + \int_{\Omega} \frac{\partial N_I}{\partial x_j} \sigma'_{ij} d\Omega + \\ + \int_{\Omega} \frac{\partial N_I}{\partial x_j} \delta_{ij} N_J d\Omega \; \bar{p}_J - \int_{\Omega} N_I b_i d\Omega - \int_{\Gamma_t} N_I t^p_i d\Gamma$$

Vectors and matrices for the continuity equation

$$M_{1_{IJ}} = \int_{\Omega} N_I \frac{1}{\kappa} N_J d\Omega \,,\;\; \boldsymbol{Q}_{IJ} = \int_{\Omega} \boldsymbol{B}^T_I \boldsymbol{m} N_J d\Omega$$

$${}^{n}g_I = \int_{\Omega} N_I \frac{1}{\kappa \Delta t} N_J d\Omega \; {}^{n}\bar{p}_J$$

where $\kappa = \left(\frac{2\mu}{3} + \lambda\right)$ and λ and μ are the Lamé constants

Box 6. Element form of the matrices and vectors of Box 5

Note that for the mixed Velocity–Pressure formulation the material part of the tangent matrix is defined by the same tangent moduli of the velocity scheme ($\boldsymbol{c}^{\sigma J}$).

In the mixed formulation, the momentum and the continuity equations can be easily decoupled. This is obtained by computing the Cauchy stress tensor using the velocities only (Eq. (2.98)) and not as the sum of its deviatoric part and the pressure (Eq. (2.99)). The uncoupled mixed Velocity–Pressure formulation is totally equivalent to the velocity formulation. In fact, although the pressures are still computed by solving the continuity equation, they do not appear in the momentum equations and, hence, they do not affect the solution for each the time step.

2.3.3 Theory of Plasticity

The theory of plasticity is dedicated to those solids that, after being subjected to a loading process, may sustain permanent (*plastic*) deformations when completely unloaded [11]. The plasticity is defined *rate-independent* if the permanent deformations of the material do not depend on the rate of application of the loads. The materials whose behavior can be adequately described by this theory are called *rate-independent plastic* materials.

Elastic-plastic laws are characterized for being path-dependent and dissipative. The stresses cannot be computed as a single-valued function of the strains because they depend on the entire history of the deformation [1].

The most important properties of the theory of plasticity can be summarized as follows:

1. The increments of strain $d\varepsilon$ are assumed to be additively decomposed into an elastic (reversible) part $d\varepsilon_{el}$ and a plastic (irreversible) part $d\varepsilon_{pl}$, such that

$$d\varepsilon = d\varepsilon_{el} + d\varepsilon_{pl} \tag{2.100}$$

2. There exists an $elastic\,domain$ where the behavior of the material is purely elastic and permanent deformations are not produced;
3. The *yield function* f_Y delimits the elastic domain. It governs the onset and the continuity of the plastic deformations and it is a functions of the state of stress and of the internal variables $\boldsymbol{q}$. So

$$f_Y = f_Y(\boldsymbol{\sigma}, \boldsymbol{q}) \tag{2.101}$$

   The yield function cannot be positive: it is negative when the stress state is below the yield value and null otherwise (*yield condition*: $f_Y = 0$);
4. The plastic strain increments are governed by the so called *flow rule*;
5. $\dot{\lambda}_{pl}$ is the *plastic strain parameter* and it is positive for a plastic loading and equal to zero for elastic loading or unloading;
6. The loading-unloading process is described by the Khun–Tucker conditions

$$\dot{\lambda}_{pl} \geq 0, \quad f_Y \leq 0, \quad \dot{\lambda}_{pl} f_Y = 0 \tag{2.102}$$

   The third condition can also be expressed in the rate form through the so-called *consistency condition*, $\dot{f}_Y = 0$. For plastic loading ($\dot{\lambda}_{pl} > 0$) the stress state lies on the yield surface ($f_Y = 0$), instead for elastic loading or unloading the yield condition is not reached ($f_Y < 0$) and there is not plastic flow ($\dot{\lambda}_{pl} = 0$).

2.3.3.1 Hypoelastic–Plastic Materials

Hypoelastic–plastic models are typically used when the elastic strains represent only a small part of the total strains. In other words, when the plastic strains are much larger than the elastic ones. This is because of the inaccuracy of the hypoelastic models in the large strain regime. However, if the elastic strains are small, the energy error introduced by the hypoelastic description of the elastic response is limited and can be considered adequate [1].

Depending on the problem, the yield function can be based on a different constitutive model. For example, for soil plasticity the Drucker–Prager model is the most used, while for porous plastic solids the Gurson model is more adequate. In this work, the J_2 *von Mises* flow model is used. This model is particularly indicated for the metal plasticity [1].

The hypoelastic–plastic model described in this section has been taken from [1]. According to the von Mises criterion [12], plastic yielding begins when the J_2 stress deviator invariant reaches a critical value. The J_2 stress deviator invariant is defined as

$$J_2 = \frac{1}{2}\sigma'_{ij}\sigma'_{ij} \tag{2.103}$$

The key assumption of the von Mises model is that the plastic flow is not affected by the pressure but only by the deviatoric stress. This hypothesis has been experimentally verified for metals [13]. For this reason the von Mises model is called to be *pressure insensitive*.

A yield function for the von Mises criterion can be defined as

$$f(\boldsymbol{\sigma}, \boldsymbol{q}) = \bar{\sigma} - \sigma_Y \tag{2.104}$$

where σ_Y is the uniaxial yield stress and it is related to the shear yield stress τ_Y as follows

$$\sigma_Y = \sqrt{3}\tau_Y \tag{2.105}$$

and in Eq. (2.104) $\bar{\sigma}$ is the *von Mises effective* or *equivalent stress* defined as

$$\bar{\sigma} = \sqrt{3J_2} \tag{2.106}$$

Concerning the deformation, the elastic-plastic decomposition described in Eq. (2.100) is rewritten in terms of rates as

$$\boldsymbol{d} = \boldsymbol{d}_{el} + \boldsymbol{d}_{pl} \tag{2.107}$$

where $\boldsymbol{d}_{el}$ and $\boldsymbol{d}_{pl}$ are the deformation rates associated to the elastic and plastic responses, respectively.

Combining Eq. (2.107) with (2.83), yields

$$\boldsymbol{\sigma}^{\nabla J} = \boldsymbol{c}_{el}^{\sigma J} : \left(\boldsymbol{d} - \boldsymbol{d}_{pl}\right) \tag{2.108}$$

The rate of plastic deformations is given by

$$\boldsymbol{d}_{pl} = \dot{\lambda}_{pl} \boldsymbol{r}(\boldsymbol{\sigma}, \boldsymbol{q}) \tag{2.109}$$

where the plastic flow rate $\dot{\lambda}_{pl}$ is a scalar and $\boldsymbol{r}(\boldsymbol{\sigma}, \boldsymbol{q})$ represents the plastic flow direction.

Substituting Eq. (2.109) in (2.108), yields

$$\boldsymbol{\sigma}^{\nabla J} = \boldsymbol{c}_{el}^{\sigma J} : \left(\boldsymbol{d} - \dot{\lambda}_{pl} \boldsymbol{r}\right) \tag{2.110}$$

During plastic loading the plastic flow rate is positive and the state of stress remains on the yield surface $f_Y = 0$. This is consistent with the third Khun–Tucker condition $\dot{\lambda} f_Y = 0$. The consistency condition $\dot{f}_Y = 0$ has the same meaning. Using the chain rule on the consistency condition, yields

$$\dot{f}_Y = \frac{\partial f_Y}{\partial \boldsymbol{\sigma}} : \dot{\boldsymbol{\sigma}} + \frac{\partial f_Y}{\partial \boldsymbol{q}} \cdot \dot{\boldsymbol{q}} = 0 \tag{2.111}$$

If the yield function depend on the invariant, the following relation holds [1, 10]

$$\frac{\partial f_Y}{\partial \boldsymbol{\sigma}} : \dot{\boldsymbol{\sigma}} = \frac{\partial f_Y}{\partial \boldsymbol{\sigma}} : \boldsymbol{\sigma}^{\nabla J} \tag{2.112}$$

Combining Eqs. (2.112) and (2.110) and substituting in Eq. (2.111), yields

$$\frac{\partial f_Y}{\partial \boldsymbol{\sigma}} : \boldsymbol{c}_{el}^{\sigma J} : \left(\boldsymbol{d} - \boldsymbol{d}_{pl}\right) + \frac{\partial f_Y}{\partial \boldsymbol{q}} \cdot \dot{\boldsymbol{q}} = 0 \tag{2.113}$$

In the most plastic models the evolution of the function $\boldsymbol{q}$ of the internal variables $\boldsymbol{h}$ can be expressed as a function of the plastic strain parameter as follows

$$\dot{\boldsymbol{q}} = \dot{\lambda} \boldsymbol{h} \tag{2.114}$$

where $\boldsymbol{h}$ are the internal variables.

Substituting Eqs. (2.109) and (2.114) in (2.113), the following relation for the plastic strain parameter is obtained

$$\dot{\lambda} = \frac{\frac{\partial f_Y}{\partial \boldsymbol{\sigma}} : \boldsymbol{c}_{el}^{\sigma J} : \boldsymbol{d}}{-\frac{\partial f_Y}{\partial \boldsymbol{q}} \cdot \boldsymbol{h} + \frac{\partial f_y}{\partial \boldsymbol{\sigma}} : \boldsymbol{c}_{el}^{\sigma J} : \boldsymbol{r}} \tag{2.115}$$

The plastic flow vector $\boldsymbol{r}$ is often derived from a plastic flow potential. If the plastic flow potential coincides with the yield function, the plastic flow is termed *associative*. In this case $\boldsymbol{r}$ is proportional to the normal of the yield surface, that is $\boldsymbol{r} \propto \frac{\partial f_Y}{\partial \boldsymbol{\sigma}}$. An

associative plastic flow has the important advantage that it can lead to a symmetric stiffness matrix [1]. In this work an associative plasticity and a constant plastic modulus H (for perfect plasticity, $H = 0$) have been considered. Using these hypotheses the plastic strain parameter is expressed as

$$\dot{\lambda} = \frac{\boldsymbol{r} : \boldsymbol{c}_{el}^{\sigma J} : \boldsymbol{d}}{H + \boldsymbol{r} : \boldsymbol{c}_{el}^{\sigma J} : \boldsymbol{r}} \tag{2.116}$$

Substituting this relation in Eq. (2.110), yields

$$\boldsymbol{\sigma}^{\nabla J} = \boldsymbol{c}_{el}^{\sigma J} : \left(\boldsymbol{d} - \frac{\boldsymbol{r} : \boldsymbol{c}_{el}^{\sigma J} : \boldsymbol{d}}{H + \boldsymbol{r} : \boldsymbol{c}_{el}^{\sigma J} : \boldsymbol{r}} \boldsymbol{r} \right) \tag{2.117}$$

The same can be computed using a tangent moduli over the whole deformation rate as

$$\boldsymbol{\sigma}^{\nabla J} = \boldsymbol{c}^{\sigma J} : \boldsymbol{d} = \left[\boldsymbol{c}_{el}^{\sigma J} - \frac{\left(\boldsymbol{c}_{el}^{\sigma J} : \boldsymbol{r} \right) \otimes \left(\boldsymbol{r} : \boldsymbol{c}_{el}^{\sigma J} \right)}{H + \boldsymbol{r} : \boldsymbol{c}_{el}^{\sigma J} : \boldsymbol{r}} \right] : \boldsymbol{d} \tag{2.118}$$

where $\boldsymbol{c}^{\sigma J}$ is the *continuum* elasto-plastic tangent modulus.

For associative plasticity, the von Mises plastic flow is computed as

$$\boldsymbol{r} = \frac{\partial f}{\partial \boldsymbol{\sigma}} = \frac{3}{2\bar{\sigma}} \boldsymbol{\sigma}' \tag{2.119}$$

Because the plastic flow vector $\boldsymbol{r}$ is deviatoric it follows that

$$\boldsymbol{c}_{el}^{\sigma J} : \boldsymbol{r} = 2\mu \quad , \quad \boldsymbol{r} : \boldsymbol{c}_{el}^{\tau J} : \boldsymbol{r} = 3\mu \tag{2.120}$$

Form Eqs. (2.86), (2.118) and (2.120), the following expression of the elastoplastic modulus is obtained

$$\boldsymbol{c}^{\sigma J} = \kappa \boldsymbol{I} \otimes \boldsymbol{I} + 2\mu \mathbf{I}' - 2\mu\gamma \boldsymbol{n} \otimes \boldsymbol{n} \tag{2.121}$$

with

$$\gamma = \frac{1}{1 + (H/3\mu)} \tag{2.122}$$

$$\boldsymbol{n} = \sqrt{\frac{2}{3}} \boldsymbol{r} \tag{2.123}$$

For perfect plasticity $H = 0$, so $\gamma = 1$ and Eq. (2.121) simplifies to

$$\boldsymbol{c}^{\sigma J} = \kappa \boldsymbol{I} \otimes \boldsymbol{I} + 2\mu \mathbf{I}' - 2\mu \boldsymbol{n} \otimes \boldsymbol{n} \tag{2.124}$$

Note that the continuum elasto-plastic tangent modulus conserves the symmetry properties of its elastic counterpart. For elastic loading or unloading, $\boldsymbol{c}^{\sigma J} = \boldsymbol{c}_{el}^{\sigma J}$.

For a plane strain state, $\boldsymbol{c}^{\sigma J}$ is

$$\left[\boldsymbol{c}^{\sigma J}\right] = \begin{bmatrix} \kappa + \frac{4}{3}\mu & \kappa - \frac{2}{3}\mu & 0 \\ \kappa - \frac{2}{3}\mu & \kappa + \frac{4}{3}\mu & 0 \\ 0 & 0 & \mu \end{bmatrix} - 2\mu\gamma \begin{bmatrix} n_{xx}n_{xx} & n_{xx}n_{yy} & n_{xx}n_{xy} \\ n_{yy}n_{xx} & n_{yy}n_{yy} & n_{yy}n_{xy} \\ n_{xy}n_{xx} & n_{xy}n_{yy} & n_{xy}n_{xy} \end{bmatrix}$$

In order to guarantee the consistency of the elastoplastic incremental scheme, the so-called *return mapping* algorithm has to be introduced. With this technique, the Khun–Tucker conditions (Eq. (2.102)) are enforced at the end of a plastic time step in order to recover exactly the yield condition $f(\sigma_{n+1}) = 0$. The return mapping algorithm consists of an initial trial elastic step followed by a plastic corrector one that is activated when the yield function takes a positive value. In Fig. 2.1 from [14], a graphical representation of the return mapping algorithm is shown.

For associative plasticity, during the plastic corrector step driven by the increment of the plasticity parameter λ, the plastic flow direction $\boldsymbol{r}$ is normal to the yield surface.

For the J_2 flow theory and associative plasticity, the return mapping is characterized to be *radial* [15]. This because the von Mises yield surface is circular, thus its normal is also radial. In Fig. 2.2 a graphical representation of the radial return algorithm for J_2 plasticity is shown.

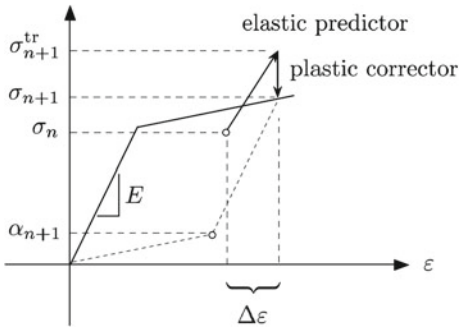

Fig. 2.1 Graphical representation of the return mapping algorithm [14]

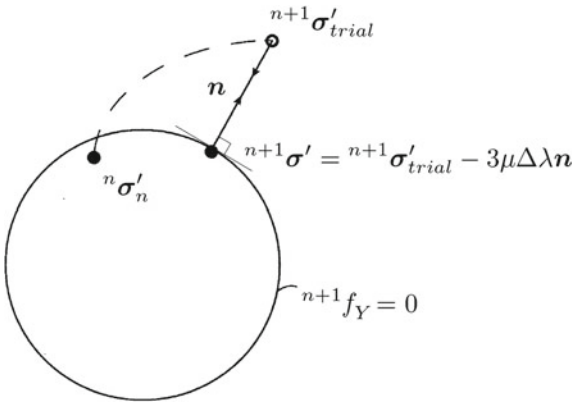

Fig. 2.2 Graphical representation of the radial return method for J_2 plasticity

The return radial mapping procedure typically starts with the elastic prediction of the stresses. This means that the linear momentum equations are solved using only the elastic part of the continuum tangent modulus (Eq. (2.86)) and the stress tensor $\boldsymbol{\sigma}^{(0)}$ is computed with Eq. (2.99) (the superindex refers to the iteration index).

Then the effective stress $\bar{\sigma}$ is computed with Eq. (2.106) and the yield function Eq. (2.104) is evaluated. If $f_Y > 0$ the return mapping iterative procedure is required. In fact, an elastoplastic step has been computed as purely elastic without fulfilling the consistency condition.

The first step of the iterative corrector procedure consists of computing the increment of the plastic parameter as

$$\delta\lambda_{pl}^{(k)} = \frac{f^{(k)}}{3\mu + H^{(k)}} \tag{2.125}$$

For perfect plasticity, the plastic modulus H is null, hence the plastic parameter is $\delta\lambda_{pl}^{(k)} = f^{(k)}/(3\mu)$.

The plastic parameter increment is updated as

$$\Delta\lambda_{pl}^{(k+1)} = \Delta\lambda_{pl}^{(k)} + \delta\lambda_{pl}^{(k)} \tag{2.126}$$

If before this step the material has never suffered plastic deformations, then $\Delta\lambda_{pl}^{(k)} = 0$.

Next the plastic strain and the internal variables are updated according to the plastic correction derived from Eq. (2.125).

The increment of plastic deformation is

$$\Delta\boldsymbol{\varepsilon}_{pl}^{(k)} = -\delta\lambda_{pl}^{(k)}\sqrt{\frac{3}{2}}\boldsymbol{n} \tag{2.127}$$

So the total plastic deformations are

$$\boldsymbol{\varepsilon}_{pl}^{(k+1)} = \boldsymbol{\varepsilon}_{pl}^{(k)} + \Delta\boldsymbol{\varepsilon}_{pl}^{(k)} \tag{2.128}$$

Once again, for the first plastic step $\boldsymbol{\varepsilon}_{pl}^{(k)} = 0$.

Next the deviatoric stresses are updated as

$$\boldsymbol{\sigma}'^{(k+1)} = \boldsymbol{\sigma}'^{(0)} - 2\mu\Delta\lambda_{pl}^{(k+1)}\boldsymbol{r}^{(0)} \tag{2.129}$$

The plastic flow direction $\boldsymbol{r}$ remains unchanged because also the tensor $\boldsymbol{n}$ remains unchanged (and radial) during the plastic corrector phase (Eq. (2.123)). This is a particular feature of the radial return mapping.

From Eqs. (2.106) and (2.130), the updated effective stress is

$$\bar{\sigma}^{(k+1)} = \bar{\sigma}^{(0)} - 3\mu\Delta\lambda_{pl}^{(k+1)} \tag{2.130}$$

Then the yield condition (Eq. 2.104) is verified again with the updated effective stress. If it is not fulfilled, the steps from Eq. (2.125) to (2.130) are repeated until $f_Y^{(k)} = 0$.

In Box 5, the return mapping algorithm for the J_2 theory and referred to a general elastoplastic time interval $[{}^{n}t, {}^{n+1}t]$ is summarized.

0. Initialization: $\varepsilon_{pl}^{(0)} = {}^{n}\varepsilon_{pl}^{(0)}, \quad \Delta\lambda^{(0)} = 0;$

1. Elastic prediction:

$$\boldsymbol{\sigma}^{\triangledown} = \boldsymbol{C}_{el}^{\sigma} : \boldsymbol{d} \rightarrow Eq.\,(2.99) \rightarrow \boldsymbol{\sigma}^{i+1}\left(\boldsymbol{\sigma}^{\triangledown}, \boldsymbol{\Omega}\right)$$

2. Evaluation of the yield function $f^{(0)} = \bar{\sigma}^{(0)} - \sigma_Y$:

$if\ f < tolerance \rightarrow$ go ahead; $\quad else$: go to loop of Step 3.

3. Plastic correction:

3.0 Initialization: $k = 0, \quad \boldsymbol{n} = \sqrt{\frac{3}{2}}\,\frac{\boldsymbol{\sigma'}}{\bar{\sigma}};$

3.1 Compute the plasticity parameter increment:

$$\delta\lambda_{pl}^{(k)} = \frac{f^{(k)}}{3\mu + H^{(k)}} \rightarrow \Delta\lambda_{pl}^{(k+1)} = \Delta\lambda_{pl}^{(k)} + \delta\lambda_{pl}^{(k)}$$

3.2 Update the plastic strains:

$$\Delta\boldsymbol{\varepsilon}_{pl}^{(k)} = -\delta\lambda_{pl}^{(k)}\sqrt{\frac{3}{2}}\boldsymbol{n} \rightarrow \boldsymbol{\varepsilon}_{pl}^{(k+1)} = \boldsymbol{\varepsilon}_{pl}^{(k)} + \Delta\boldsymbol{\varepsilon}_{pl}^{(k)}$$

3.3 Update the stresses:

$$\boldsymbol{\sigma}'^{(k+1)} = \boldsymbol{\sigma}'^{(0)} - 2\mu\Delta\lambda_{pl}^{(k+1)}\sqrt{\frac{3}{2}}\,\boldsymbol{n}$$

$$\bar{\sigma}^{(k+1)} = \bar{\sigma}^{(0)} - 3\mu\Delta\lambda_{pl}^{(k+1)}$$

3.4 Check the yield condition $f^{(k+1)} = \bar{\sigma}^{(k+1)} - \sigma_Y$:

$if\ f^{(k+1)} < tolerance \rightarrow$ converged;

$else$: $k \leftarrow k + 1$ and go to Step 3.1.

Box 5. Radial return mapping for J_2 plasticity

2.3.4 Validation Examples

In this section several problems are studied in order to validate and the V and the VP elements and to make interesting comparisons. First an example for small displacements is studied. Then a benchmark problem for non-linear solid mechanics, namely the Cook's membrane, is analyzed. The third example is a uniformly loaded circular plate and it involves also plasticity. All these examples are analyzed in statics considering a unique unit time step increment for the velocity-based formulations. The last example is solved in dynamics and for both the hypoelastic and hypoelastic–plastic models.

Simply Supported Beam

The first validated problem is a simply supported beam loaded by its self-weight. The problem has been studied in statics so the inertial forces have not been considered. The geometry of the problem is illustrated in Fig. 2.3 and the problem data are given in Table 2.1. The material properties of the structure can be assimilated to the ones of a structural steel.

The beam undergoes small displacements under the effect of its self-weight, hence linear elastic theory is suitable for computing a reference solution. The accuracy of the formulation is tested by comparing the computed values for the maximum vertical displacement and the maximum XX-component of the Cauchy stress tensor with the values given by a linear elastic analysis. According to this theory, both maximum values are reached in the central section of the beam and they are computed as

$$U_Y^{max} = \frac{5gHL^4}{384EI} = 1.5348 \cdot 10^{-4}\ m \tag{2.131}$$

$$\sigma_X^{max} = \frac{3gHL^2}{4H^2} = 2887818\ Pa \tag{2.132}$$

Fig. 2.3 Simply supported beam. Initial geometry

Table 2.1 Simply supported beam. Problem data

L	5 m
H	0.5 m
Young modulus	196 GPa
Density	$7.85 \cdot 10^3$ kg/m^3
Poisson ratio	0

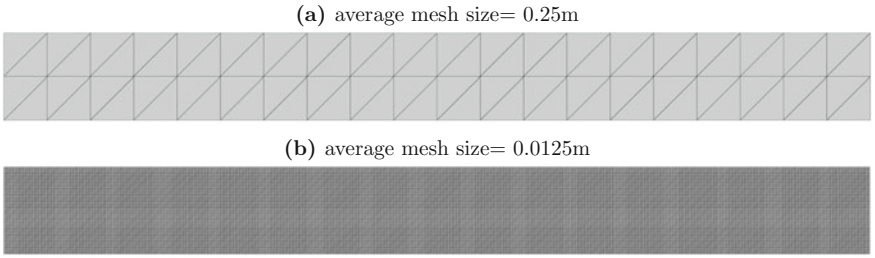

Fig. 2.4 Simply supported beam. Coarsest and finest meshes used for the analysis

The problem has been solved in 2D using both the Velocity and the mixed Velocity–Pressure formulations using 3-noded triangular elements. The static problem is solved with only one unit time increment.

In order to verify the convergence of both schemes, the problem has been solved using structured meshes of 3-noded triangles with the following average sizes: 0.25, 0.125, 0.05, 0.025, 0.0125 m. In Fig. 2.4 the finest (mesh size = 0.00125 m, 32,000 elements) and the coarsest (mesh size = 0.25m, 80 elements) meshes are illustrated.

In Fig. 2.5 the solutions for the vertical displacement and the XX-component of the Cauchy stress tensor computed at the Gauss points obtained with the mesh with average size 0.025 m are plotted.

For the visualization of all the numerical results of this work the pre-postprocessor software GID [16] has been used.

Table 2.2 collects the values of the maximum vertical displacement (absolute value) and the XX-component of the Cauchy stress tensor computed at the Gauss point using the V-element and the VP-element for different FEM mesh.

In the examples presented in this section, for the convergence analysis the percentage error is computed versus the solution obtained with the finest discretization as

$$error = abs\left(\frac{value_{finest\ mesh} - value_{tested\ mesh}}{value_{finest\ mesh}}\right) \cdot 100 \tag{2.133}$$

For example, the maximum vertical displacement obtained with the finest mesh (average size 0.0125 m) is the reference solution for both V and VP elements. The convergence curves for both formulations are plotted in Fig. 2.6. Both elements show a quadratic convergence rate for this error measure.

Compressible Cook's Membrane

The Cook's membrane is a benchmark problem for solid mechanics. The static problem is solved twice in this thesis. In this section a compressible material is considered; in the next chapter the nearly incompressible case is analyzed. In both cases the problem has been solved with only one unit time increment.

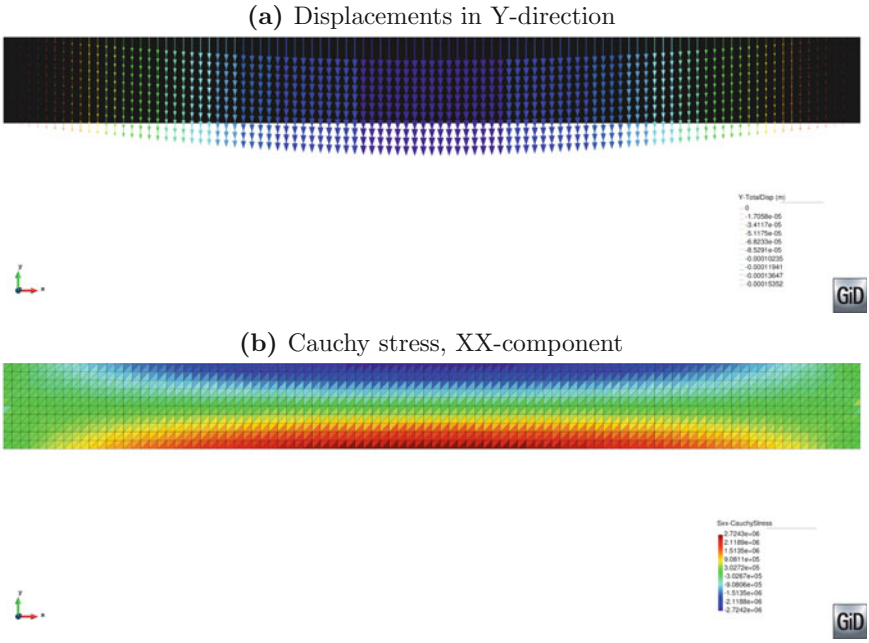

Fig. 2.5 Simply supported beam. Numerical results

Table 2.2 Simply supported beam. Cauchy stress XX-component and maximum vertical displacement for different discretizations

Mesh size	**V-element**		**VP-element**	
	σ_x^{max}	U_y^{max}	σ_x^{max}	U_y^{max}
2.50E-01	1.46E+06	9.92E-05	1.53E+06	8.41E-05
1.25E-01	2.29E+06	1.37E-04	2.37E+06	1.29E-04
5.00E-02	2.72E+06	1.54E-04	2.80E+06	1.52E-04
2.50E-02	2.82E+06	1.56E-04	2.87E+06	1.56E-04
1.25E-02	2.86E+06	1.57E-04	2.89E+06	1.57E-04

The initial geometry of the problem, as well the problem data are given in Fig. 2.7a.

The self weight of the membrane has not been taken into account in the analysis, so the membrane deforms under only the effect of the external load applied at its free edge. In this case the structure undergoes large displacements and the solution cannot been computed analytically. The results taken as the reference ones are those published in [17]. The comparison with the mentioned publication, as well the convergence test are performed for the vertical displacement of point A of Fig. 2.7a with coordinates $(x, y) = (48, 52)$. According to [17], under plane stress conditions this displacement is $U_Y^{max} = 23.964$.

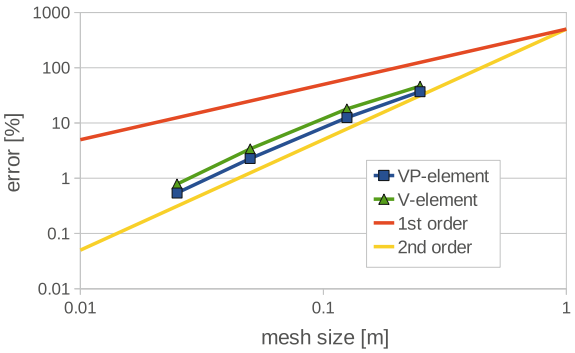

Fig. 2.6 Simply supported beam. Convergence analysis for the maximum vertical displacement for V and VP elements

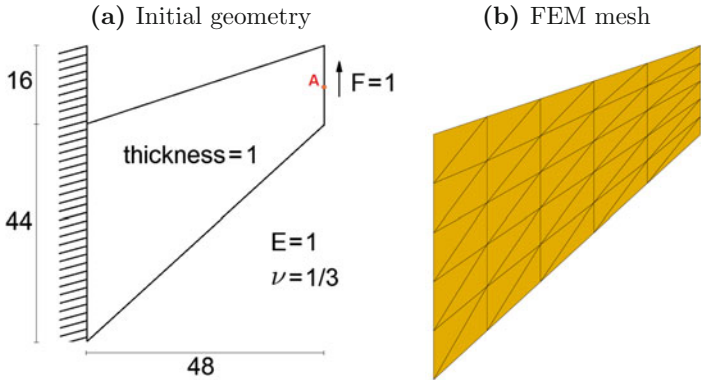

Fig. 2.7 Cook's membrane. Initial geometry, material data and FEM mesh (5 subdivisions for each edge corresponding to 50 elements)

The domain is discretized with a structured mesh and the edges of the membrane have the same number of partitions. In Fig. 2.7b one of the meshes used for this problem is given. The figure refers to the case of 5 elements for each edge of the membrane.

For the 2D simulation a convergence study has been performed using various discretizations. In the finest one the edges have 200 subdivisions, while in the coarsest one only 2.

The 3D problem (thickness $= 1$) has been solved for an unstructured mesh with average size 0.5 only. The results for this mesh are given in Fig. 2.8, where the XX-component of the Cauchy stress tensor is plotted over the deformed configuration.

For the 3D simulation, the vertical displacements at the central point of the free edge for the V and the VP elements are 23.942 and 23.952, respectively, which correspond to an error versus the reference solution of 0.092 % for the V-element and 0.050 % for the VP-element.

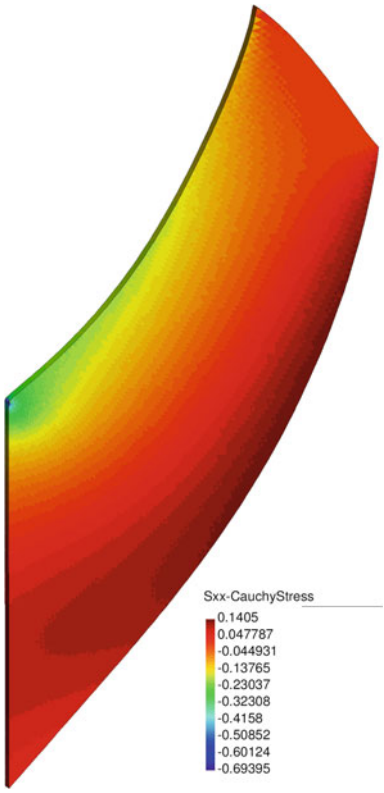

Fig. 2.8 Cook's membrane. Numerical results for the 3D simulation: the XX-component of the Cauchy stress tensor is plotted over the deformed configuration

The vertical displacement of point A of Fig. 2.7a obtained for all the 2D discretizations and for both the Velocity and the Velocity–Pressure formulations is plotted in the graph of Fig. 2.9.

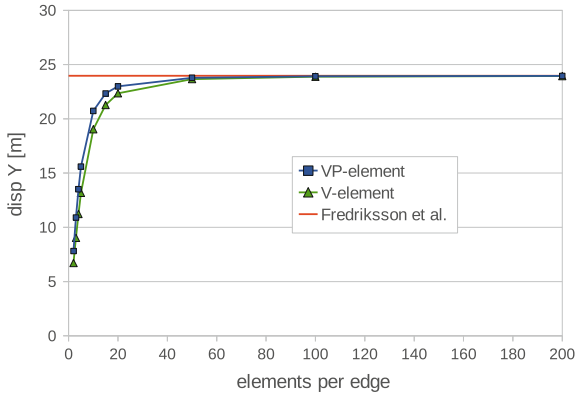

Fig. 2.9 Cook's membrane. Vertical displacement of point A of Fig. 2.7a. Results for V and VP elements compared to the reference solution [17]

Table 2.3 Cook's membrane. Maximum vertical displacement for different discretizations

Elements per edge	**V-element**	**VP-element**
	U_y^{max}	U_y^{max}
2	6.707	7.8105
3	9.0274	10.901
4	11.232	13.515
5	13.1755	15.5985
10	19.037	20.729
15	21.272	22.332
20	22.349	22.987
50	23.658	23.781
100	23.878	23.913
200	23.941	23.95

In Table 2.3 the numerical values are given.

The convergence curves are given in Fig. 2.10. Also in this case the convergence rate is quadratic for both formulations.

Uniformly Loaded Circular Plate

The problem analyzed in this section is a simply supported circular plate subjected to a uniform pressure P on its top surface. The plate constrains are applied on its lower edge. The plate has a radius $R = 10$ and thickness $h = 1$. In this work, the axial symmetry of the problem has not been used, and the plate has been analyzed in 3D using 4-noded tetrahedra. The average size for the tetrahedra is 0.175. This gives 214,047 nodes. In Fig. 2.11 the FEM mesh used is shown.

A hypoelastic–perfectly plastic model has been used, and the problem has been solved with the mixed velocity pressure formulation. For the plastic part, a von Mises yield criterion has been considered. The plate has Young modulus $E = 10^7$, Poisson

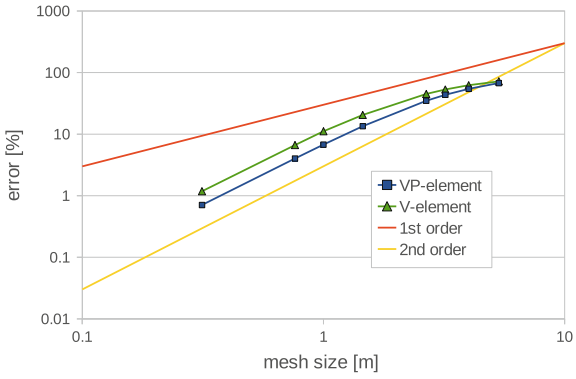

Fig. 2.10 Cook's membrane. Convergence analysis for the vertical displacement of point A of Fig. 2.7a for the V and VP elements, V-element and VP-element, respectively

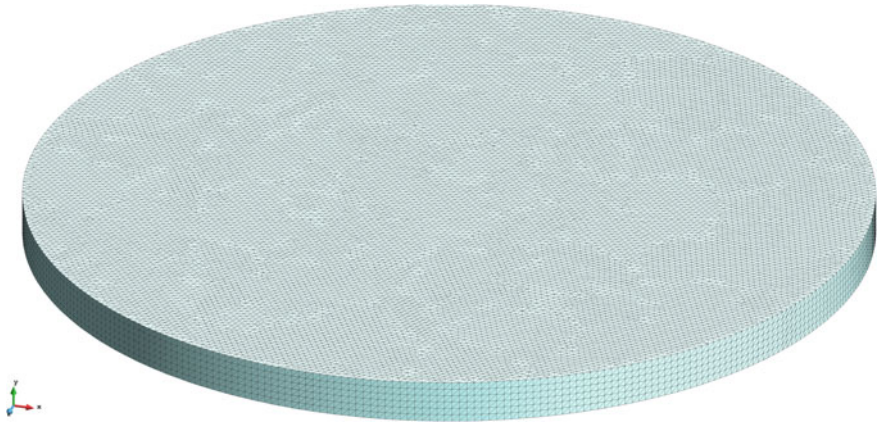

Fig. 2.11 Uniformly loaded circular plate. Initial geometry and 3D FEM used [18]

ratio $\nu = 0.24$ and a uniaxial yield stress $\bar{\sigma}_y = 16{,}000$. The objective of the study is to determine the limit load for the plate. Using the procedure described in [19], the limit load can be computed analytically by combining the limit analysis and the finite difference method. According to this theory, the limit load can be approximated as

$$P_{lim} \approx \frac{1.63\bar{\sigma}_y h^2}{R^2} = 260.8 \tag{2.134}$$

The same problem was solved in [11] using eight-noded axisymmetric quadrilateral elements with four Gauss integration points. The limit load obtained with a relatively coarse mesh (10 finite elements distributed in two layers across the thickness) is $P_{lim}^{FE} = 259.8$ [11].

As in [11], the limit load has been considered as the one for which the non-linear procedure cannot longer converge for a small increment of the load.

In Fig. 2.12 the maximum vertical displacement of the plate is plotted against the pressure on the top surface. In Table 2.4 the numerical values are given.

For the present analysis the limit load obtained is $P_{lim} = 264.27$, the relative percentage errors with respect the solutions given in [11, 19] are 1.37 % and 1.76 %, respectively.

In Fig. 2.13 the vertical displacements are depicted over the deformed configuration obtained with the limit load. The plate central section is highlighted in the picture.

In Fig. 2.14 some snapshots of the von Mises effective stress are plotted over the central section of the plate for the different load conditions. The picture shows clearly the progressive evolution of the plastic zone.

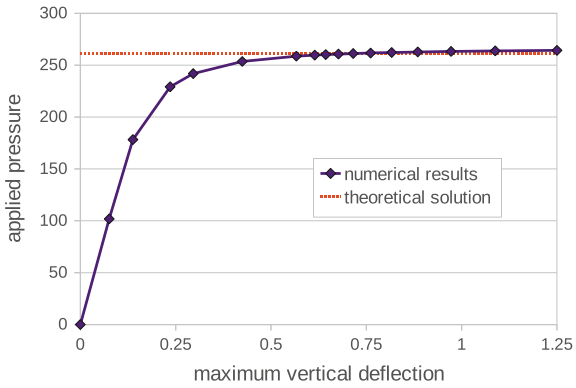

Fig. 2.12 Uniformly loaded circular plate. Maximum deflection versus the applied pressure [18]

Table 2.4 Uniformly loaded circular plate. Numerical values of the maximum vertical deflection for different applied pressures

Pressure	Max. deflection	Pressure	Max. deflection
101.84	0.0758	260.71	0.677
178.22	0.138	261.21	0.716
229.14	0.236	261.73	0.761
241.87	0.296	262.24	0.816
253.58	0.424	262.73	0.885
258.67	0.567	263.26	0.972
259.69	0.615	263.77	1.088
260.20	0.644	264.27	1.250

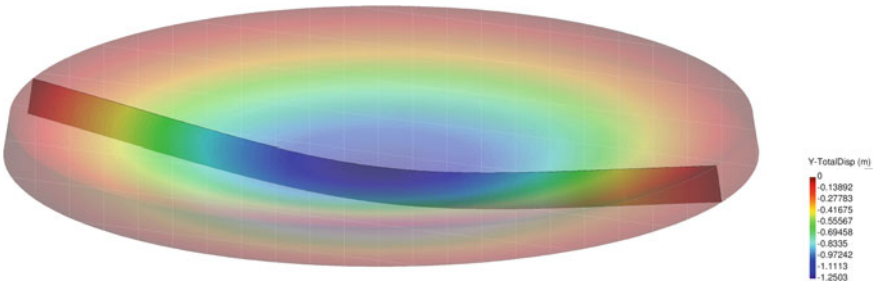

Fig. 2.13 Uniformly loaded circular plate. Vertical displacement contours for the maximum pressure sustained by the plate ($P_{lim} = 264.27$) [18]

Plane Strain Cantilever in Dynamics

The plane strain cantilever illustrated in Fig. 2.15 has been chosen as the reference case for a large displacement dynamics analysis. The problem data are in given in Table 2.5. The problem was introduced and studied in [20]. In the reference publica-

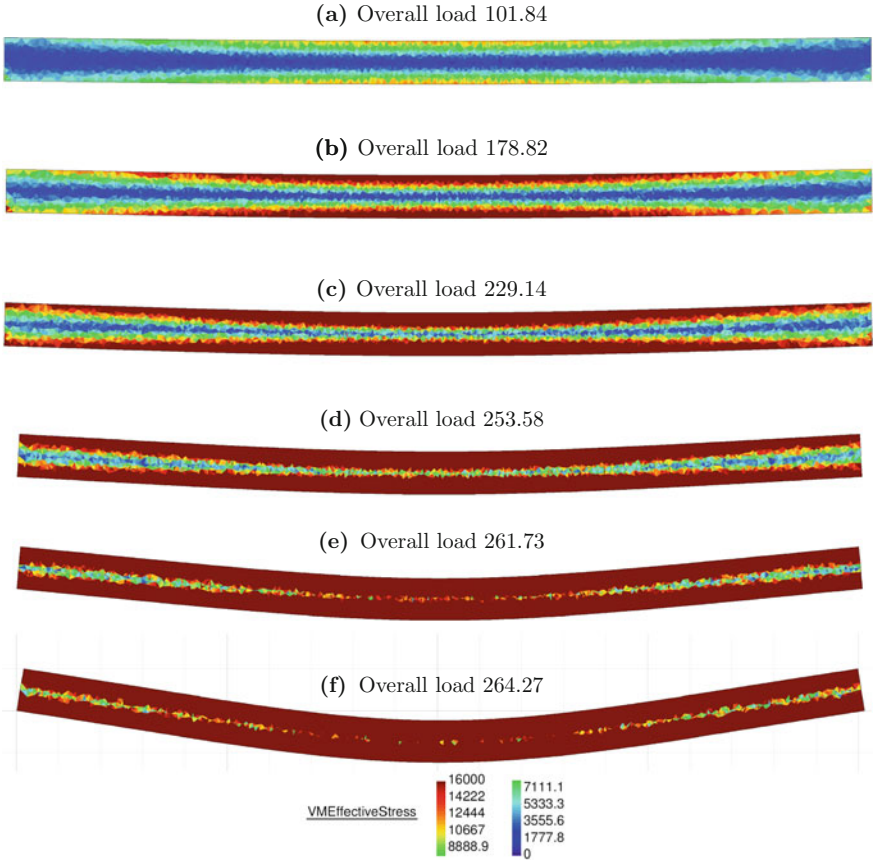

Fig. 2.14 Uniformly loaded circular plate. Von Mises effective stress over the deformed configurations for different load conditions (only the central section is depicted) [18]

tion, the load was applied as a step function at time $t = 0\,\mathrm{s}$ and its magnitude was defined by the equation $f = 15(1 - y^2/4)$ where y is the coordinate in the direction of the load. However, in this analysis the load has been considered uniformly distributed over the free edge (the overall value is 40, as in [20]).

The problem has been solved with both a hypoelastic and a hypoelastic–plastic models. First the results of the hypoelastic model are given.

Hypoelastic Model

The problem has been solved in 2D and 3D and using both the V and VP elements. In order to simulate the plane strain state, in the 3D analysis the nodal displacements in the transversal direction to the load have been constrained [20].

The reference solution is the elastic one given in [20].

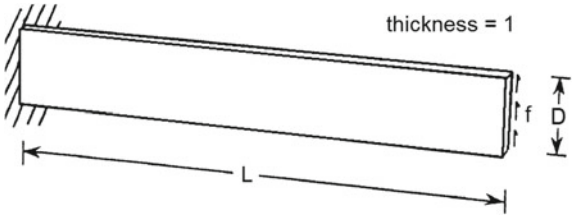

Fig. 2.15 Plane strain cantilever. Initial geometry

Table 2.5 Plane strain cantilever. Problem data

L	25
D	4
Young modulus	10^4
Poisson ratio	0.25

For the 2D analysis a convergence study has been performed. Structured finite element meshes have been used and the coarsest and the finest ones have a mean size of 1 and 0.125, respectively. Both meshes are given in Fig. 2.16.

For the 3D case, the problem has been solved with the finest mesh only (average size for the 4-noded tetrahedra equal to 0.125). The results for the 3D case obtained with the VP-element are illustrated in Fig. 2.17 where the pressure contours are plotted over the deformed configuration.

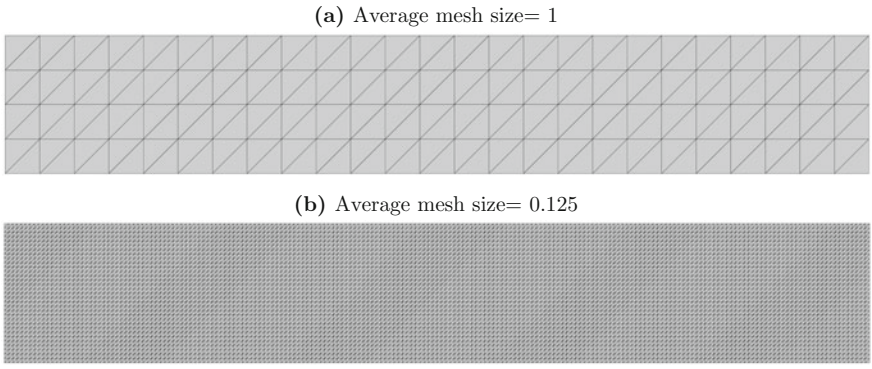

Fig. 2.16 Plane strain cantilever. Coarsest (mesh size = 1, 200 elements) and finest meshes (mesh size = 0.125, 12,800 *triangles*) used for the 2D analysis

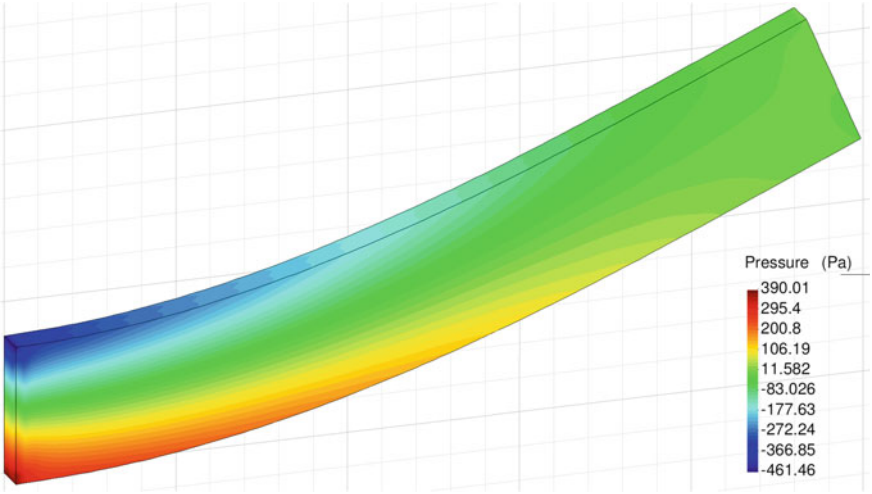

Fig. 2.17 Plane strain cantilever. Numerical results for the 3D simulation obtained with the VP-element: pressure contours plotted over the deformed configuration [18]

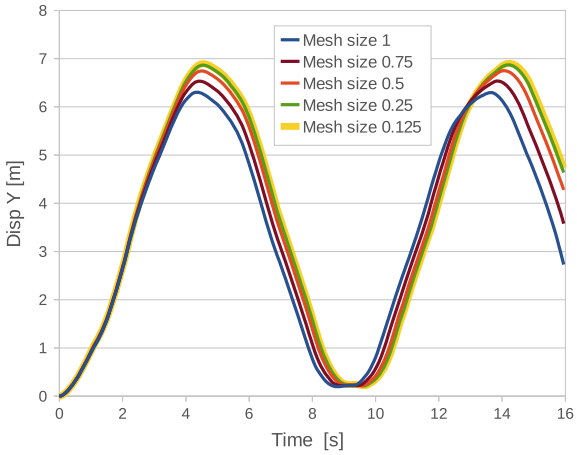

Fig. 2.18 Plane strain cantilever. Time evolution of the top corner vertical displacement for different 2D discretizations. Results obtained with the VP-element [18]

In Fig. 2.18 the time evolution of the top corner vertical displacement is plotted for each of the FEM meshes. These results have been obtained with the VP-element.

According to [20], the maximum vertical displacement is $U_Y^{max} = 6.88$. Table 2.6 collects the maximum vertical displacement obtained with the V and the VP elements for all the meshes.

Table 2.6 Plane strain cantilever. Maximum top corner vertical displacement for different 2D discretizations

Mesh size	**V-element**	**VP-element**
	U_y^{max}	U_y^{max}
1	5.759	6.306
0.8	6.144	6.534
0.5	6.568	6.743
0.25	6.811	6.863
0.125	6.875	6.895

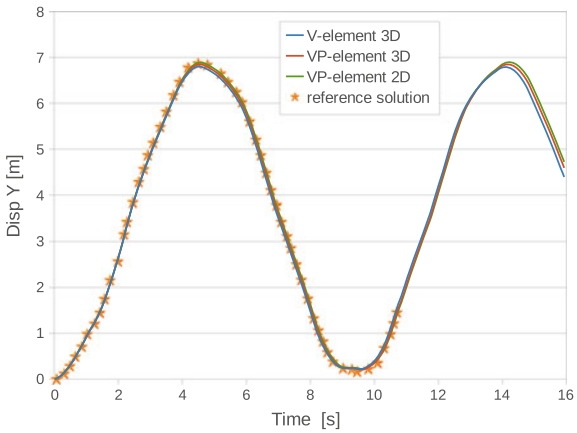

Fig. 2.19 Plane strain cantilever. Time evolution of the top corner vertical displacement. Solutions for the 2D VP-element and the 3D V and VP elements obtained with the finest mesh (average size 0.125) compared to the reference solution [18, 20]

The four curves of Fig. 2.19 are the converged time evolution of the top corner vertical displacement obtained with the V-element in 3D, the VP-element in 2D and 3D and the reference solution [20]. The curves corresponding to the V and VP elements are almost superposed and they match the reference solution.

Hypoelastic–plastic model

The same problem has been solved for an elastic-plastic material with linear hardening. The yield stress is 300 and the plastic modulus H is 100. The problem has been solved with the mixed Velocity–Pressure formulation and by using structured meshes, as the ones of Fig. 2.16. The reference solution is taken from [20] where the benchmark was proposed. In [20] the converged value for the maximum top corner vertical displacement is 8.22. The hypoelastic–plastic mixed Velocity–Pressure

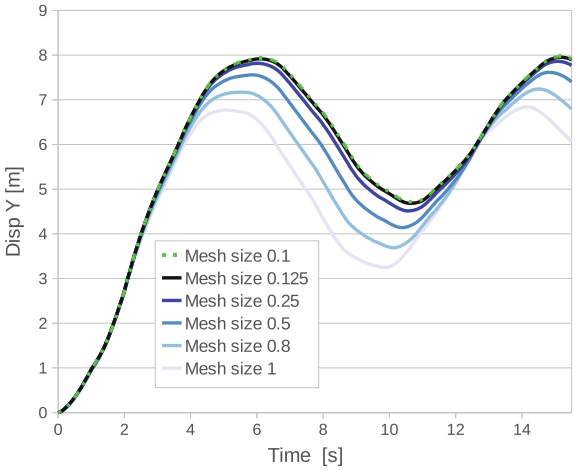

Fig. 2.20 Plane strain elastoplastic cantilever. Time evolution of the top corner vertical displacement for different 2D discretizations [18]

Table 2.7 Plane strain elastoplastic cantilever. Maximum and residual top corner vertical displacements for different discretizations

Mesh size	U_y^{max}	U_y^{res}
1	6.77	3.25
0.8	7.17	3.69
0.5	7.56	4.14
0.25	7.82	4.51
0.125	7.92	4.68
0.1	7.94	4.72
0.0625	7.97	4.77

formulation converges to 7.97 (error of 2.998 %). In the graph of Fig. 2.20 the time evolution of the top corner vertical displacement is plotted for the different FEM meshes.

In Table 2.7 the numerical values for the maximum and the residual top corner vertical displacements are given for each of the FEM mesh.

The problem has been solved also for the 3D problem for a structured mesh of 4-noded tetrahedra with average size 0.125.

In Fig. 2.21 the von Mises effective stresses are plotted over the deformed configuration at the time instant when the top corner vertical displacement is reached ($t = 6.05$ s).

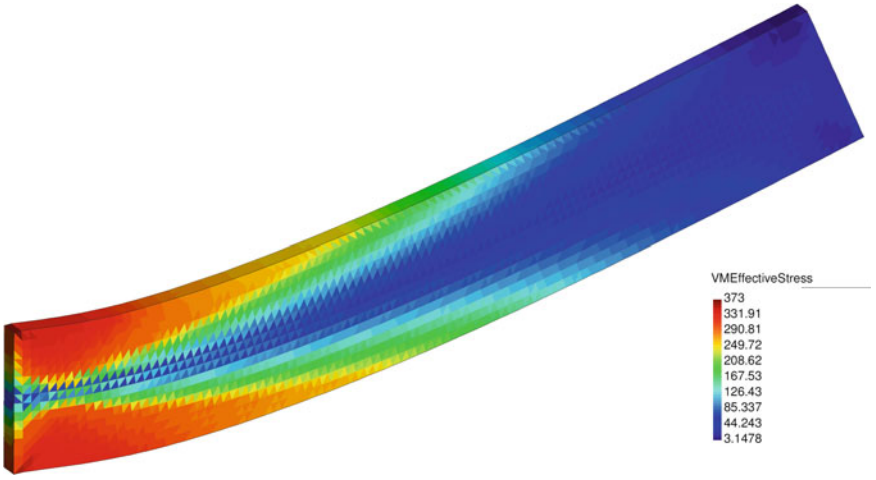

Fig. 2.21 Plane strain elastoplastic cantilever. Numerical results for the 3D simulation. Von Mises effective stress plotted over the deformed configuration at ($t = 6.05\,\mathrm{s}$) [18]

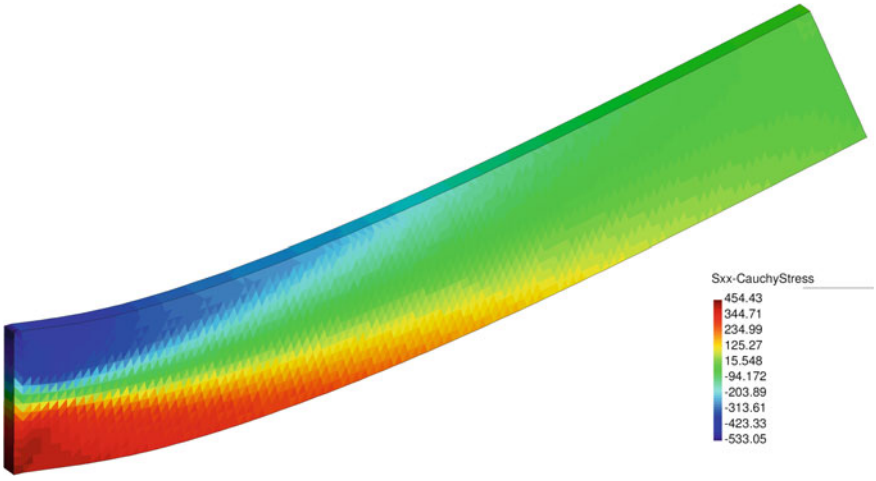

Fig. 2.22 Plane strain elastoplastic cantilever. Numerical results for the 3D simulation: XX-component of the Cauchy stress tensor plotted over the deformed configuration at ($t = 6.05\,\mathrm{s}$) [18]

In Fig. 2.22 for the same time instant the XX-component of the Cauchy stress tensor is plotted.

In Fig. 2.23 the 3D solution is compared to the 2D results obtained with a structured mesh with the same average size. The curves coincide almost exactly.

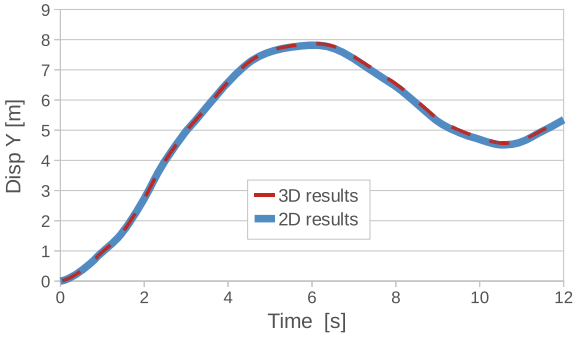

Fig. 2.23 Plane strain elastoplastic cantilever. Time evolution of the top corner vertical displacement. Numerical results for the 2D and the 3D simulations for the same average mesh size (0.125) [18]

2.4 Summary and Conclusions

In this chapter two velocity-based finite element Lagrangian procedures, namely the Velocity and the mixed Velocity–Pressure formulations, have been derived for a general compressible material.

The derivation of both formulations has been carried out with the aim of maintaining the scheme as general as possible. The mixed Velocity–Pressure formulation has been derived exploiting the linearized form of the Velocity formulation. In particular, it has been shown that the tangent matrix of the linear momentum equations is the same for both schemes.

The mixed Velocity–Pressure procedure is based on a two-step Gauss–Seidel solution algorithm. First, the linear momentum equations are solved for the velocity increments, next the continuity equation is solved for the pressure in the updated configuration. At the end of these steps the convergence for the velocities and the pressure is checked. Linear interpolation has been used for both velocity and pressure fields.

Next, both formulations have been particularized for hypoelastic solids. The finite elements generated from the Velocity formulation and the mixed Velocity–Pressure formulations have been called V and VP element, respectively.

The numerical scheme for dealing with J_2 associative plasticity has been also given.

Several numerical examples have been given for validating the V and VP elements for large displacements dynamics problems involving both hypoelastic and hypoelastoplastic compressible solids. It has been shown that both elements are convergent for all the numerical examples analyzed.

References

1. T. Belytschko, W.K. Liu, B. Moran, and K.I. Elkhodadry. *Nonlinear Finite Elements For Continua And Structures. Second Edition.* John Wiley & Sons, New York, 2014.
2. O.C. Zienkiewicz and R.L. Taylor. *The Finite Element Method. Its Basis and Fundamentals. (6th Ed.)*. Elsevier Butterworth-Heinemann, Oxford, 2005.
3. F. Brezzi. On the existence, uniqueness and approximation of saddle-point problems arising from lagrange multipliers. *Revue française d'automatique, informatique, recherche opérationnelle. Série rouge. Analyse numérique*, 8 (R-2):129–151, 1974.
4. C. Truesdell. Hypo-elasticity. *Journal of Rational Mechanics and Analysis*, 4,1, 1955.
5. C. Truesdell. Remarks on hypo-elasticity. *Journal of research of the National Bureau of Standards - B. Mathematics and Mathematical Physics*, 67B (3):141–143, 1963.
6. C. Truesdell. The simplest rate theory of pure elasticity. *Communications on Pure and Applied Mathematics*, 8:123–132, 1955.
7. G.A. Holzapfel. *Nonlinear Solid Mechanics. A continuum Approach for Engineering*. John Wiley & Sons, New York, 2000.
8. C. Truesdell and W. Noll. *The Non-Linear Field Theories of Mechanics, Volume III*. Springer, New York, 2004.
9. J.C. Simo and T.J.R. Hughes. *Computational Inelasticity*. Springer, New York, 1998.
10. W. Prager. *Introduction to Mechanics of Continua*. Ginn and Company, Boston, 1961.
11. E.A. De Souza Neto, D. Peric, and D.R.J. Owen. *Computational methods for plasticity. Theory and applications*. John Wiley & Sons, New York, 2008.
12. R. von Mises. Mechanik der festen körper im plastisch- deformablen zustand. *Nachrichten von der Gesellschaft der Wissenschaften zu Göttingen, Mathematisch-Physikalische Klasse*, pages 582–592, 1913.
13. P. Bridgmain. *The Physics of High Pressure*. Bell & Sons, London, 1949.
14. R.I. Borja. *Plasticity. Modeling & Computation*. Springer, New York, 2013.
15. J.C. Simo and R.L. Taylor. Consistent tangent operators for rate-independent elastoplasticity. *Computer Methods in Applied Mechanics and Engineering*, 48:101–118, 1985.
16. GiD website. http://www.gidhome.com.
17. M. Fredriksson and N.S. Ottosen. Fast and accurate four-node quadrilateral. *International Journal For Numerical Methods In Engineering*, 61:1809–1834, 2004.
18. A. Franci, E. Oñate, and J. M. Carbonell. Velocity-based formulations for standard and quasi-incompressible hypoelastic-plastic solids. *International Journal for Numerical Methods in Engineering*, doi:10.1002/nme.5205., 2016.
19. J.J. Skrzypek. Plasticity and creep. theory, examples, and problems. *CRC Press*, London, 1993.
20. T. Belytschko and L.P. Bindeman. Assumed strain stabilization of eight node hexahedral element. *Computer Methods In Applied Mechanics And Engineering*, 105:225–260, 1993.

http://www.springer.com/978-3-319-45661-4

Unified Lagrangian Formulation for Fluid and Solid Mechanics, Fluid-Structure Interaction and Coupled Thermal Problems Using the PFEM

Franci, A.

2017, XIX, 211 p. 168 illus., 147 illus. in color.,
Hardcover
ISBN: 978-3-319-45661-4